www.sciencemag.org/cgi/content/full/science.aao0645/DC1

Supplementary Materials for

Morphogen gradient reconstitution reveals Hedgehog pathway design principles

Pulin Li,* Joseph S. Markson,* Sheng Wang, Siheng Chen, Vipul Vachharajani, Michael B. Elowitz†

*These authors contributed equally to this work.
†Corresponding author. Email: melowitz@caltech.edu

Published 5 April 2018 on *Science* First Release
DOI: 10.1126/science.aao0645

This PDF file includes:

Other Supplementary Material for this manuscript includes the following:
(available at www.sciencemag.org/cgi/content/full/science.aao0645/DC1)

Materials and Methods – Experiments

Cell culture and reagents

NIH3T3 cells were obtained from ATCC (CRL-1658). All the subsequent cell lines were derived from the parental NIH3T3 cells. All cells were cultured in DMEM supplemented with 10% Calf Serum (ThermoFisher/Hyclone, #SH30087), 1x Pen/Strep/Glutamine (Gibco, #10378-016), and 1 mM Sodium Pyruvate (Gibco, #11360070). For regular cell line maintenance, cells were passaged every 3 days at 1:10. For all the assays, receiver cells were grown into 100% confluency before being stimulated with ligands or spatially patterned to form gradients. To reduce the background fluorescence, colorless FluoroBrite DMEM (ThermoFisher, #A18967) with 10% Calf Serum was used for all the time-lapse image acquisition.

Engineering stable cell lines

All transgenes were cloned into the PiggyBac transposon system (System Biosciences), which allows more efficient genomic integration of multiple vectors simultaneously (Table S3). All constructs were transfected into cells facilitated by PiggyBac transposase and Lipofectamine LTX (ThermoFisher, #15338100). Cells stably integrated with the corresponding constructs were selected and enriched with the following antibiotics: Hygromycin (InvivoGen, #ant-hg, 300 μg/ml), Blasticidin (InvivoGen, #ant-bl, 10 μg/ml), Puromycin (Gibco, #A11138-03, 3 μg/ml), and Geneticin (Gibco, #10131-35, 600 μg/ml). In cases where two different constructs were co-transfected simultaneously, a sequential antibiotic selection procedure (alternating between the two antibiotics every 2-3 days) was used to enrich for double-positive polyclonal population. Then clonal population was selected and characterized upon single-cell limiting dilution. The details about the cell lines are described below:

- SHH senders: To control SHH expression in an inducible fashion, a mutant estrogen receptor was fused to GAL4 (ERT2-GAL4), which enables the activation of the UAS promoter by adding (Z)4-Hydroxytamoxifen (4-OHT, Sigma, #H7904) (*29*).
- Wild-type receivers: To report the intracellular signaling activity, a transcription-based reporter was created by using 8 tandem copies of GLI binding sequence (GBS)(*10*) and a minimal CMV promoter to control the expression of H2B-Citrine (Fig. S1).
- *Ptch1-/-* receivers (Fig. S3): In the wild-type receiver background, both alleles of the endogenous *Ptch1* were knocked out using CRISPR (Table S4, Fig. S3). Multiple guide RNA sequences were tested, and the one targeting the intron-exon junction produced the highest knockout efficiency.
- Open loop receivers (Figs. 2A, S3): To create feedback-free cells, ectopic expression of PTCH1 was restored in *Ptch1-/-* receivers using Tet-3G inducible system (Life Technologies) (*30, 31*). Tet-3G is constitutively expressed under the control of *PGK* promoter. *TRE* promoter controls the expression of *Ptch1*, the level of which can be tuned by Doxycycline (Dox, Clontech, #631311). Clones with basal leaky expression of PTCH1 from the *TRE* promoter sufficient to suppress the pathway autoactivation were selected.
- PTCH1-SynFB receivers (Figs. 4A, S13): In *Ptch1-/-* receivers, ectopic expression of PTCH1 was restored under the control of *TRE* promoter (*32*, *33*). Clones with basal leaky expression of PTCH1 from the *TRE* promoter sufficient to suppress the pathway autoactivation were selected. Tet-3G level is controlled by the SHH pathway activity using the same *GBS* promoter that drives the Citrine reporter expression. Dox concentration controls the amount of PTCH1 expression for a given level of Tet-3G, and thus the feedback strength.
- PTCH1-ΔLoop2-SynFB (Figs. 4E, S14): Dox-tunable synthetic feedback circuit was integrated into the wild-type receivers. Clones with complete absence of basal leaky expression of Ptch1-ΔLoop2 was selected.

Recombinant proteins and chemicals

Recombinant mouse Sonic Hedgehog (rmSHHN) N-terminus (R&D, #464-SH-025) was dissolved in 1x Dulbecco PBS with 0.1% BSA. SMO activator Purmorphamine (Cayman Chemical, #10009634) and cell cycle inhibitor Roscovitine (Selleckchem, #S1153) were dissolved in DMSO.

Reconstitution of morphogen gradient *in vitro*

All gradient formation experiments were performed in 24-well tissue culture-treated μ-Plate (ibidi, #82406). Radial gradients were set up by mixing senders and receivers at a 1:1000 ratio, and thus individual senders were randomly distributed and spatially separated. 600,0000 cells were plated per well to force contact inhibition and cellular quiescence, which is required for NIH3T3 cells to become responsive to SHH stimulation. Linear gradients were set up using PDMS culture inserts (ibidi, #80209). 100,000 senders were seeded in a single rectangular space for 4-6 hrs. In situation where the sending strength of senders needs to be tuned, senders were mixed with wild-type NIH 3T3 cells at various ratios. Wild-type cells do not express any HH ligands. Once the senders adhere to the plate, inserts were removed and 600,000 receivers were plated in the same well. All gradients were set up the night before, and cells were induced at corresponding 4-OHT and/or Dox concentrations the next morning to initiate morphogen production and gradient formation. All cells were grown in DMEM media containing 10% serum throughout the course of gradient formation, and media was replaced every 12-24 hrs.

Time-lapse fluorescence microscopy

All time-lapse images were acquired on an inverted Olympus IX81 fluorescence microscope with Zero Drift Control (ZDC), an ASI 2000XY automated stage, iKon-M CCD camera (Andor, Belfast, NIR), and a 20x dry objective (0.7NA). Fluorophores were excited with an X-Cite XLED1 light source (Lumen Dynamics). Cells were kept in a custom-made environmental chamber enclosing the microscope, with humidified 5% CO_2 flow at 37°C. Microscope and image acquisition were controlled by Metamorph software (Molecular Devices). Imaging usually started 2-3 hrs upon ligand stimulation or sender induction. Images were taken every 30 min, typically for 48–72 hrs. For radial gradients, senders were chosen randomly during the setup stage based on the following pre-established criteria: single senders are well separated from each other and away from the well edges by at least 300 μm. Senders that remained as single cells without proliferation or death during the entire period were used for data analysis. The fraction of senders that stayed undivided and alive varies between 30 - 60%, depending on the initial cell density, cellular states and environmental conditions. Therefore, 20-30 individual senders were usually recorded for each experimental condition. For linear gradients, only the sender-receiver interface along the outer edge of the ibidi well were used for all experiments. The length of the interface typically allows selection of 7 fields of view without overlapping between adjacent fields, and avoiding regions where senders invaded receiver fields or non-straight sender-receiver interfaces. Generally, data from all fields of view were used for further analysis unless the sender-receiver interface shifted significantly over time due to uneven local cell densities and/or cell migration, which usually counts <3% of all data.

Although the reconstituted system is three-dimensional (Fig. S2E), diffusive processes operate along each dimension independently. The widefield microscopy used for imaging signaling gradients effectively measures a 2D projection of the 3D cell layer. This allows us to focus on transport in the *x-y* plane, which is the most relevant for these spatial patterning processes

Quantitative analysis of linear SHH signaling gradients

All image analysis was performed using customized Matlab program.

- ***Automatic boundary detection*:** Senders were labeled with nuclear-localized mTurquoise2. Each pixel in the image (*T(x,y,t)*) was identified as mTurquoise positive (*1*) or negative (*0*) based on a fixed threshold above background. Sender density in space (*T_mean(x,t)*) was calculated by summing up the total mTurquoise pixel values along each column, orthogonal to the direction of the ligand diffusion. An average sender density profile was calculated by taking the temporal mean at all x positions

(*T_mean2(x)*), and fit to a Hill-like function $a \times b^n / (b^n + x^n)$, with n ≥ 5. The position at which *T_mean2(x) = 0.2a* was defined as the boundary location.

- ***Image normalization:*** To quantify the SHH signaling gradient in space and time, two normalization procedures were applied: (1) Background subtraction: media auto-fluorescence and camera background were imaged in media-only wells (*F_back(x,y)*) and subtracted from the raw data (*F_raw(x,y,t)*); (2) Field flattening: to assess the uniformity of illumination within the field of view in the Citrine and mCherry channels, wells containing FITC and Alexa Fluor 647 dyes in the media were imaged (*F_standard(x,y)*). All raw data were normalized:

$$F(x,y,t) = (F\_raw(x,y,t) - F\_back(x,y)) / (F\_standard(x,y) - F\_back(x,y))$$

- ***Quantification of temporally integrated signaling activity in time and space*:** Signaling gradient in space measured by Citrine fluorescence intensity was calculated by the mean of all pixel values along each column, orthogonal to the direction of ligand diffusion. A smoothing procedure was then applied, both spatially and temporally. The transcriptional activity of the Citrine reporter comprises two components: (1) basal promoter activity due to the basal leaky activity of *8xGBS-miniCMV*, which is GLI-, and thus SHH pathway-, independent; (2) SHH signal-induced activity, which is GLI-, and thus SHH pathway-, dependent. Because the GLI-dependent activity is what counts for the signaling gradient, we subtracted the Citrine signal due to the basal activity, which was deduced from the cells outside the gradient, at each corresponding timepoint.
- ***Calculation of instantaneous signaling activity:*** The Citrine fluorescence reporter is fused to Histone H2B, which concentrates and stabilizes Citrine in the nuclei. The rate of Citrine fluorescent protein accumulation follows $\partial Citrine/\partial t = \alpha - \gamma \cdot Citrine$, in which α is the production rate of Citrine and γ is its degradation rate constant. Because H2B-Citrine is very stable and cell proliferation is minimal under the high-confluency condition, γ is close to 0. As a result, $\partial Citrine/\partial t$ approximately equals α. α is controlled by the transcriptional activity of GLI, which is a direct readout of the SHH pathway signaling activity. Therefore, total Citrine represents temporally integrated signal activity, and its time derivative represents instantaneous signaling activity (Figs. 2C, 4C, S1-4).
- ***Quantification of gradient properties, e.g. amplitude, lengthscale and time to reach steady state (τ):*** Amplitude and lengthscale were calculated based on total Citrine, which represents temporally integrated signaling activity (Figs. 2E, 4D-E, S4). Amplitude is defined as the Citrine intensity closest to the boundary. Lengthscale is defined as the distance over which the gradient drops to 1/*e* of its amplitude. Calculation of the time to reach steady state *(τ)* is based on the spatio-temporal dynamics of instantaneous signaling activity. The signaling activity is generally stabilized at all positions with unavoidable fluctuations after 30 hrs (Fig. 2C). Therefore, at any position, its mean signaling activity between 30 hr and the end of the movie approximates its steady state signaling activity (Fig. S4C). τ is defined as the earliest timepoint at which the signal intensity at the 50% decay length (the position at which the signal is 50% of the gradient amplitude) first reaches 90% of its steady-state value.

Quantitative analysis of radial SHH signaling gradients

The same image normalization procedure used in linear gradient analysis was applied to radial gradients. Single senders separated from each other by at least 300 μm were manually identified, and a single pixel was chosen as the center of the gradient. Concentric rings with single-pixel increment in the radius (*r*) were drawn around the gradient center (Fig. 1D, *schematic*). Mean fluorescence intensity per pixel within each annulus was calculated (*F_mean(r,t)*) and smoothed. *F_mean(r, t)* always exhibits nonmonotonic behavior: increasing and then decreasing with respect to *r* (space). This is because a single sender usually takes up an area of 10 x 10 pixels in the middle of the gradient, and the actual gradient does not start at *r=0*. Therefore, we re-defined the gradient boundary as the position at which *F_mean(r)* is at its maximum value at the last timepoint. The rest of the data analysis used similar procedures as the linear gradient.

Testing the route of ligand movement

To distinguish between two potential mechanisms of gradient formation (bulk diffusion through media vs. movement within the cell layer), we performed the following experiments:
(I) Rocker experiment: Radial gradients were set up in 24-well plates in duplicate, with one plate on a still shelf and the other on a rocker (Boekel Scientific, Rocker II Model 260350). Rocker was rocking at the frequency of ~1 Hz. Both plates were incubated in the same tissue culture incubator with appropriate temperature, humidity and CO_2 control. Gradients were imaged and quantified at 48 hrs after 4-OHT induction.
(II) Gap experiment: A 0.15 mm thick coverglass (VWR #48380068) was cut into two pieces with a 1:8 ratio of surface area and coated with Hamster fibronectin (Oxford Biomedical, #CH30) at a concentration of 5 µg/ml overnight. Senders were plated on the smaller piece and receivers on the larger piece. Once the cells were confluent, the two pieces of the same coverglass were placed in a single well of a 6-well plate and aligned such that the two pieces are in direct contact with each other ('contact mode'), or with a gap of approximately 30 µm in between ('gap mode'). In the contact mode, senders and receivers form a continuous monolayer culture. In the gap mode, senders and receivers cannot cross the gap to reach each other, neither there is a continuous extracellular matrix between the two cell populations. To prevent the coverglass from moving, the outer corners of the coverglass were fixed onto the bottom of the plate with agarose. Gradients were imaged at 48 hrs after 4-OHT induction, on the EVOS FL Auto Cell Imaging System (ThermoFisher, #AMF4300) and a 10x objective.

We noticed that a fraction of secreted ligands could escape from the monolayer cell into the culture media. However, such 'free' ligands in the media get mixed quickly in the entire well due to diffusion and convection. To keep the SHH concentration in the media below the threshold required for receiver activation, we kept the sender-receiver ratio as low as possible, the media volume as high as possible, and frequently changed the media (every 12 hrs). Frequent media change did not prevent gradient formation, further suggesting that the ligand in the media is not responsible for gradient formation.

Estimation of the speed of signaling gradient formation
Using the spatio-temporal dynamics of the signaling gradient activity (Fig. S2A), the speed of signaling gradient formation was estimated based on the Mean Squared Displacement (msd). By plotting the instantaneous signaling activity $\partial\text{Citrine}(x,t)/\partial t$ as a function of space (x), the msd ($< x(t)^2 >$) at different timepoints (t) can be calculated:

$$< x(t)^2 > = \sum \left((\partial\text{Citrine}(x,t)/\partial t) \times x^2 \right) / \sum \left(\partial\text{Citrine}(x,t)/\partial t\right)$$

D_{eff} can be estimated by taking linear regression of msd vs. time with a delay Δt:

$$< x(t)^2 > = 2 \times D_{eff} \times (t - \Delta t)$$

There are two points worth being noticed: (1) The linear regression is based on the assumption that time delay Δt is independent of the ligand concentration, but rather an inherent kinetic feature of the downstream signal transduction and transcriptional activation by GLI proteins. This assumption is supported by the time-lapse movies of receiver response dynamics with bath treatment of rmSHHN, in which the length of time delay does not appear to depend on the ligand concentration (figs. S3D, 13C); (2) The estimated D_{eff} does not directly measure ligand diffusion, but rather the rate of signaling activity spreading in the cell layer. The value of D_{eff} depends on several factors, including the ligand diffusion rate, the level of ligand and receptor, and the input/output function of SHH signal processing. Nevertheless, it offers an order-of-magnitude estimation about the speed of gradient formation, comparable to those measured *in vivo* for HH and other morphogens (*32-34*).

Analysis of signaling activity and cell movement at the single-cell level
In order to separate out individual nuclei while maintaining cellular responsiveness to SHH stimulation, we diluted signaling reporter-containing receiver cells with 'dark' wild-type NIH3T3 cells at 1:50 ratio. 150,000 cells in total were plated per well in tissue culture-treated 96-well µ-plate (ibidi, #89626). Cells were allowed to adhere overnight. rmSHHN or Purmorphamine were added to the media at 0 hr, and time-lapse movies were recorded under the same condition as the gradient movies. Individual nuclei were segmented, tracked and quantified for total Citrine fluorescence using customized programs (*35*). Promoter activity was calculated by taking the time-derivative of total Citrine (Fig. S1C). The spatial displacement of each cell relative to its position

at time 0 was calculated along the direction of gradient formation (x-axis in Fig. S2B). The squared displacement versus time is biphasic, with faster cell movement during the first 12 hrs and slower movement later. This behavior was quantified with a piecewise linear regression. The speed of cell movement is estimated by the slope of the regression (Fig. S2B-C). In both phases, the speed of cell movement is less than 10% of the speed of signaling gradient formation, suggesting cell movement plays an insignificant role in gradient formation. Similar results were obtained when the cell movement was analyzed along the y-axis, orthogonal to the direction of gradient formation (data not shown).

Analysis of signaling dynamics at the population level with bath SHH treatment

150,000 signaling reporter-containing receiver cells were plated per well in tissue culture-treated 96-well µ-plate (ibidi, #89626). Cells were allowed to adhere overnight. rmSHHN or Purmorphamine were added to the media at 0 hr, and time-lapse movies were recorded under the same condition as the gradient movies. Similar normalization and quantification procedures used for the analysis of 1D gradients were applied to the data without tracking individual cells (Figs. S3D, S13C).

Flow cytometry

Samples for flow cytometry analysis were harvested using 0.05% Trypsin (Life Technologies), resuspended in 1x HBSS (Hank's Balanced Salt Solution, Life Technologies) with 2.5 mg/ml BSA (Sigma, A4503), and filtered through 40 µm strainers (BD Falcon) to remove aggregates. Fluorescence intensity was analyzed on a MACSQuant VYB flow cytometer (Miltenyi Biotec, Bergisch Gladbach, Germany). Data were analyzed with a custom Matlab program (EasyFlow, available upon request)(*35*).

Quantitative RT-PCR

We used quantitative RT-PCR to compare the synthetic reporter expression with endogenous SHH pathway target expression. Wild-type NIH3T3 cells containing the GBS-H2B-Citrine reporter were treated with different concentrations of rmSHHN for 24 hrs and lysed. Standard RNA extraction protocols with on-column DNase I digestion (Qiagen, #79254) using RNeasy mini kits (Qiagen, #74106) were performed. The concentration of extracted RNA was analyzed with NanoDrop and 500 ng RNA was used for a standard 20 µl iScript (Bio-Rad) reverse transcription reaction. 0.5 µl of the resulting cDNA was used for a 10 µl qPCR reaction (iQ SYBR Green Supermix, Bio-Rad, #1708880) on a CFX96 Real-Time Thermal Cycler (Bio-Rad). Each reaction had ≥2 technical replicates, with mouse *Tbp* as housekeeping control. The calculated ΔΔCq values (log2 fold change) for each gene (*Gli1, Ptch1*, and *Citrine*) across all rmSHHN concentrations were normalized between 0-1. Relative fold change of endogenous targets was plotted against relative fold change of *Citrine* (Fig. S1D). Primer sequences are provided in Table S4.

RNA-seq and data analysis

Wild-type NIH3T3 cells were grown to 100% confluency before vehicle control or 20 nM rmSHHN treatment in regular culture media. Total mRNA was purified after 48 hrs. Library was constructed according to standard Illumina protocols. Sequencing was performed on a HiSeq 2500 sequencer. Two biological samples for each condition were pooled together for sequencing. Data analysis was performed with a local instance of Galaxy (*36*), aligned to mm10 mouse reference genome. A standard analysis pipeline included Tophat, Cufflinks and Cuffdiff (*37*).

Materials and Methods - Modeling

Simulations

Framework

In order to closely tie experiment and modeling, we designed our models to approximate experimental conditions. The open loop system (Eqs. C.1-8) (*17*) and closed-loop PTCH feedback system (Eqs. D.1-5)(*17*) are each described by a set of five coupled, nonlinear partial differential equations, with the SHH ligand being the

only mobile species; other closed-loop systems (IC, EC, and uncoupled feedback) are modeled according to the same framework.

We modeled gradient formation in one dimension across a receiver field 1000 μm wide by discretizing space into a 1000-element vector, with each element representing a virtual "cell" of width 1 μm. HH enters the receiver field at a constant flux α_{HH} from the left-hand side. At the right-hand side, the system has an open (i.e., absorptive) boundary condition, mimicking the experimental setup, in which the receiver field stretches across several millimeters before reaching the side wall of the well. Diffusion was modeled as hops between adjacent elements, turning the five coupled partial differential equations into a set of 1000*5 = 5000 coupled ordinary differential equations. Simulations of these coupled ODEs were performed in MATLAB (R0216a) using the `ode15s` solver.

Simulations proceed in three steps: (1) pre-equilibration, (2) gradient simulation, and (3) gradient characterization. The same framework was used for more complex models incorporating full-length GLI, GLIA, GLI2 and GLI3, and/or adaptive behavior via GLI downregulation (supplementary text sections E-G).

Pre-equilibration

We assume that the concentrations of HH pathway components (*P*, *C*, *R*, and where appropriate, *I* and *E*) are at steady-state prior to initiation of HH production in the senders. This steady state is uniform in space and corresponds to the solution of the differential equations with $H = 0$ everywhere (note that this yields $C = 0$ everywhere). For each simulation, we computed the steady-state solution analytically or by simulating the system forward in time until a steady state is reached. A system is deemed to be at steady state at time t_i if, over the subsequent 4.5 hr, none of the species except for *S* (which accumulates continuously) changes by more than 0.1% (Eq. H.5). After pre-equilibration, *S* is reset to zero.

Gradient simulation

The pre-equilibrated system constitutes the initial conditions for gradient simulation. At time $t = 0$, inward flux of SHH was turned on and the simulation was run forward in time, recording the concentration of each species every 30 min. Simulations presented in Fig. 2 and Figs. S5-6 were run for a fixed duration of 48 hr, the same length as the corresponding experiments. In these figures, we present results for *S*, the integrated signal, as this is what is measured experimentally. For simulations in Fig. 3 and Figs. S7-11, we analyzed the instantaneous signal $\partial S/\partial t$ in order to focus on the steady-state properties of the gradients. This choice is based on the fact that $\partial S/\partial t$, but not *S*, is invariant to the length of the simulation and the dynamics of approach to steady state. Here, we defined steady-state stringently (Eq. H.5): a system is deemed to be at steady state at time t_i if, over the subsequent 4.5 hr, none of the species except for *S* (which accumulates continuously) changes by more than 0.1% (Eq. H.5). Note that the measure "time to each steady state (τ)" is defined differently (Eq. H.6) to facilitate experimental measurement. τ is the earliest timepoint at which signaling activity at λ_{50} [the distance, after the system has stabilized (Eq. H.5), at which the instantaneous signaling activity is 50% of its maximum] first reaches 90% of its final value. We examined whether the decay lengthscale cutoff (50%, 37%, etc.) affects the conclusions about model performance and found that, except for cutoffs near 100%, PTCH feedback always produces the fastest τ (or ties for fastest with another architecture).

Gradient Characterization

After completion of each simulation, we computed metrics to characterize the signaling gradients (supplementary text section H). Lengthscale (λ) is defined as the distance over which the gradient drops to $1/e$ of its highest value (Eqs. H.1-2). Amplitude (*A*) is defined as the signal intensity at the first "cell" (Eqs. H3-4). The time to reach steady state (τ) is the earliest timepoint at which the signal intensity at the 50% decay length (the position at which the signal is 50% of the gradient amplitude) first reaches 90% of its steady-state value (Eq. H.6).

The sensitivity $\sigma_{y,\alpha_{HH}}$ of a metric *y* to α_{HH} is defined as the log change in the metric divided by the log change in α_{HH} (Eq. H.7). Practically, sensitivity was computed by calculating *y* at a particular value of α_{HH} and at twice that value of α_{HH}, with all other parameters held constant; with such a two-fold increase in α_{HH}, the sensitivity reduces simply to the fractional change in the metric itself.

Gradient shape was quantified with a shape factor θ, defined as the length of the second third of the gradient (i.e., the distance over which $\partial S/\partial t$ decreases from ⅔ to ⅓ of the gradient amplitude) divided by the length of the first third of the gradient at steady state (Fig. 3E, Eq. H.8). Because lengths are quantized (taking on only integer values in microns), the θ versus α_P curve is inherent choppy. To emphasize the underlying trend, we smoothed the curves in 3E using `lowess` smoothing with a window of 0.25.

Parameter fitting

Open loop fitting

Parameters for the GLIR-only, GLIA+GLIR, and GLI2+GLI3 models were determined by bounded least-squares fitting (figs. S5B-D, S6B-C, and data not shown) to open loop experimental data. Parameter bounds (figs. S5D and S6C) were chosen based on prior experimental measurements or computational models (*38-43*). Fitting proceeded in two steps. First, the parameters describing the cell-autonomous species — i.e., *P*, *C*, *R*, and *S* for the GLIR-only model — as well as the interaction of *P* with *H* (Eqs. C.1-5, E.1-4, F.1-4) were determined by a global fit to the rmSHHN dose titration data (Fig. S1B) using the `lsqnonlin` function, with residuals weighted by the standard deviation of each datapoint (Figs. S5B, S6B). Fits were initialized 10-15 times with parameter guesses randomly and uniformly distributed in log space between the lower and upper bounds (Figs. S5D, S6C). We chose the parameter set resulting in the lowest weighted sum of squared residuals. Next, we fitted the spatial model (Eqs. C.6-8) to the observed gradient formation dynamics in the open loop system for four different α_{HH}, all at 1x α_{PTC} (Figs. S5C, S6B). In this spatial fit, we fixed the parameters determined from the 0D fit and floated the newly-introduced parameters – *D*, γ_H, and α_{HH}, as well as a multiplicative factor *m* relating the 0D and 1D data amplitudes. Fits were run 10-15 times with parameter guesses randomly and uniformly distributed in log space between the lower and upper bounds. We chose the parameter set resulting in the lowest weighted sum of squared residuals. The first-order degradation term for *H* (Eq. C.6) was included to encapsulate constitutive degradation of *H* as well as loss to the media. Notably, $\gamma_H << k_{on}*P$ at the lowest value of *P* at steady state, implying that *H* depletion occurs predominantly through binding to *P*.

Determination of feedback strengths

The PTCH feedback strength β was calculated to match the experimentally-observed 7-fold upregulation of PTCH production (reported by mCherry promoter activity) in receivers located at the sender-receiver boundary for relative α_{HH} = 1.0. Given the other system parameters, a feedback strength β = 36 in the GLIR-only model yields an approximately seven-fold increase in PTCH production at relative α_{HH} = 1.0. Feedback strengths for the IC and EC models (β_I = 4.7 and β_E = 12) in Fig. 3 were chosen to produce the same amplitude or lengthscale, respectively, as the PTCH model at relative α_{HH} = 0.0625; note that because the IC and EC models each have only one tunable parameter, it is not possible to match *both* the amplitude and lengthscale to the values obtained by PTCH feedback. Those values of β_I and β were used for the uncoupled model in Fig 3. Feedback strengths used in other figures are noted in the figure.

Supplementary Text

A. Dependence of HH pathway activation on the receptor states: Free-Receptor Model vs. Ratio Model

How HH pathway activity depends on states of the PTCH receptor has been debated in previously published studies. Taipale *et al.* suggested that free PTCH catalytically suppresses pathway activity ('Free-Receptor Model') *(44),* whereas Casali *et al.* proposed that signal activity depends on the ratio between ligand-bound and free PTCH ('Ratio Model') *(45)*. We analyzed the two opposing models mathematically and compared them with our experimental observations. Our results support the Free-Receptor Model. The details of the calculation are included in this section.

We constructed the models to match the conditions of the experiments with which we will compare them – specifically, bath treatment of open loop receivers with recombinant mouse SHH (Fig. S2C). We assume that ligand (*H*) and receptor (*P*) bind reversibly to form a complex (*C*) with a dissociation constant K_d.

$$H + P \overset{K_d}{\leftrightarrow} C$$

Because *H* is in a large volume of media, the concentration of *H* stays constant despite its consumption by receivers. The dynamics of *P* and *C* are

$$\frac{dP}{dt} = \alpha_P - \gamma_P P - k_{on} HP + k_{off} C \tag{A.1}$$

$$\frac{dC}{dt} = k_{on} HP - k_{off} C - \gamma_C C \tag{A.2}$$

where the production rate of *P* is α_P, the rate constant for the degradation of *P* is γ_P, and the rate constant for the degradation of *C* is γ_C. Solving for the steady state of Eqs. A.1-2 results in

$$\alpha_P - \gamma_P P - \gamma_C C = 0. \tag{A.3}$$

Assuming the binding and unbinding between *H* and *P* quickly reaches equilibrium, then by definition

$$\frac{HP}{C} = K_d. \tag{A.4}$$

From Eqs. A.3-4, free PTCH is

$$P = \frac{\alpha_P K_d}{\gamma_P K_d + \gamma_C H} \tag{A.5}$$

and the ratio between ligand-bound PTCH (*C*) and free PTCH (*P*) is

$$\frac{C}{P} = \frac{H}{K_d}. \tag{A.6}$$

In the Free-Receptor Model, because PTCH negatively regulates the intracellular signal (*S*), we model *S* as

$$S = A \frac{{K_P}^n}{{K_P}^n + P^n} \tag{A.7}$$

in which *A* is a scaling factor representing the maximum signal activity, K_P is the concentration of *P* at which signal is half maximal, and *n* is the Hill coefficient. With Eqs. A.5 and A.7, the relationship between *S* and *H* in a bath treatment at steady state can be derived as

$$S = A \frac{(\gamma_P K_d + \gamma_C H)^n}{(\gamma_P K_d + \gamma_C H)^n + \left(\frac{\alpha_P K_d}{K_P}\right)^n}. \tag{A.8}$$

In the Ratio Model, we assume that the intracellular signal *S* depends on the ratio *C*/*P*,

$$S = A\frac{\left(\frac{C}{P}\right)^n}{{K_C}^n + \left(\frac{C}{P}\right)^n} \quad \text{(A.9)}$$

where K_C is the ratio of *C*/*P* at which signal is half maximal, and *n* is the Hill coefficient. With Eqs. A.6 and A.9, the relationship between S and H in a bath treatment at steady state can be calculated as

$$S = A\frac{H^n}{H^n + (K_C K_d)^n}. \quad \text{(A.10)}$$

Comparing Eqs. A.8 and A.10, we see that the two models make different predictions about the relationship between *S* and *H.* The Free-Receptor Model predicts that the dose response curve of *S* vs. *H* depends on PTCH production rate (α_P), while the Ratio Model predicts that the dose response curve does not depend on α_P. Our experimental results (Fig. S3C) show that the dose response curve depends on α_P, consistent with the results of Taipale *et al. (44)*, and thus support the Free-Receptor Model.

B. Ratiometric dependence of signaling gradient features on HH and PTCH production rates: a toy model

We observed experimentally that both the amplitude and lengthscale of SHH signaling gradients in open loop receivers depend ratiometrically on the ligand and receptor production rates (Figs. 2E-F, S4D, S5F). In this section, we use a toy model to show that the "double-negative" logic of the core HH signaling pathway (Fig. 1B) is sufficient to generate the ratiometric behavior, under two assumptions: (1) the first-order degradation of free ligand (*L*) is much larger than degradation through receptor-mediated internalization (an assumption needed to obtain analytical results); and (2) the ligand concentration near the source (L_0) is much higher than the ligand-receptor dissociation constant (K_d), which is necessary for the formation of long-range gradients, as the majority of receptors near the boundary must be bound to ligand in order to prevent free receptor from retarding mobility of the ligand. The "double-negative" logic of the HH pathway in which ligand binding to the receptor PTCH relieves PTCH's inhibitory effect on intracellular signaling is in contrast to the more prevalent "double-positive" pathway architecture associated with morphogen pathways such as BMP and FGF, in which ligands activate receptors by forming ligand-receptor complexes, which in turn activate the intracellular signal. Under the same assumptions, in a double-positive toy model, signaling gradient amplitude depends only on the receptor production rate, while lengthscale depends on the product of ligand and receptor production rates. The details of this analysis are described below.

The key difference between the "double-negative" vs "double-positive" pathways is the dependence of signaling activity on the abundance of free or ligand-bound receptors, respectively. Therefore, we first estimated the spatial profile of free receptor (*R*) and ligand-receptor complex (*C*) at steady state. Under the assumption that the distribution of *L* is unaffected by receptor binding, *L(x)* follows a stereotypical exponential decay profile in space (*x*) at steady state *(46)*:

$$L(x) = L_0 e^{\frac{-x}{\lambda_L}} \quad \text{(B.1)}$$

with amplitude

$$L_0 = \frac{j_0}{\sqrt{D\gamma_L}} \quad \text{(B.2)}$$

and lengthscale

$$\lambda_L = \sqrt{D/\gamma_L}\,, \quad \text{(B.3)}$$

where D is the ligand diffusion coefficient, j_0 is the ligand flux at the left boundary and γ_L is the first order ligand degradation rate constant. In this approximation, cells passively sense the local ligand concentration through ligand (L)-receptor (R) binding that results in formation of a ligand-receptor complex (C) with a dissociation constant K_d so that

$$L(x) + R(x) \overset{K_d}{\leftrightarrow} C(x).$$

We assume that ligand-receptor binding and unbinding are sufficiently fast that complex formation is at equilibrium, and that C and R degrade with the same rate constant (γ_R). If R is produced at rate α_R, and degraded at rate γ_R, the total level of receptor per cell R_0 is

$$R_0 = \frac{\alpha_R}{\gamma_R}, \tag{B.4}$$

and the distributions of free receptor R and complex C at steady state are

$$R(x) = R_0 \frac{K_d}{K_d + L(x)} \tag{B.5}$$

$$C(x) = R_0 \frac{L(x)}{K_d + L(x)}. \tag{B.6}$$

In the "double-negative" model, signal $S(x)$ inversely depends on the level of free receptor $R(x)$

$$S(x) = \frac{K}{K + R(x)} \tag{B.7}$$

where K is the concentration of R at which the signal reaches half maximum. Prior to initiation of gradient formation, signaling in the receivers is negligible, i.e., $S(0) \approx 0$, which requires $R_0 >> K$. Without loss of generality, we assume that the Hill coefficient equals 1. The amplitude of the signal gradient is defined as the signal in the cell closest to the source. Based on Eqs. B.1, B.4 and B.6, with the assumption of $L_0 >> K_d$ at $x = 0$, then

$$S(0) = \frac{K}{K + \frac{R_0 K_d}{L_0}}. \tag{B.8}$$

Signal gradient decay length λ_S is defined as

$$S(\lambda_S) = \frac{S(0)}{e}. \tag{B.9}$$

With Eqs. B.1, B.2, B.3, B.5 and B.7, and the assumption of $L_0 >> K_d$ and $R_0 >> K$, we obtain

$$e^{\frac{-\lambda_S}{\lambda_L}} \approx \frac{K_d}{eK_d + (e-1)K\frac{L_0}{R_0}}$$

and thus,

$$\lambda_S \approx \lambda_L \ln\left(\frac{eK_d + (e-1)K\frac{L_0}{R_0}}{K_d}\right). \tag{B.10}$$

Based on Eqs. B.2 and B.4, the ratio of total receptor and ligand concentrations at x=0 follows

$$\frac{R_0}{L_0} \propto \frac{\alpha_R}{\alpha_L}. \tag{B.11}$$

Because λ_L is independent of α_L by assumption (Eq. B.3) and K_d is a constant, we find that amplitude $S(0) \propto \alpha_L/\alpha_R$ and lengthscale $\lambda_S \propto \alpha_L/\alpha_R$ both depend on the ratio of ligand to receptor production rates.

In the "double-positive" model, signal $S(x)$ depends on the ligand-bound receptor $C(x)$ as

$$S(x) = \frac{C(x)}{K + C(x)}. \quad \text{(B.12)}$$

K is the concentration of *C* at which signal is half-maximal. Without loss of generality, we assume that the Hill coefficient equals 1. The amplitude of the signal gradient can be calculated based on Eqs. B.1, B.6 and B.12, at *x = 0* as

$$S(0) = \frac{L_0 R_0}{L_0 R_0 + K(L_0 + K_d)}.$$

Assuming that $L_0 >> K_d$, the signal gradient amplitude can be approximated as

$$S(0) = \frac{R_0}{K + R_0} \quad \text{(B.13)}$$

and signaling gradient decay length λ_S, defined in Eq. B.9 and with Eqs. B.1-2, B.5 and B.12, can be approximated as

$$\lambda_S \approx \lambda_L \ln\left(\frac{(e-1)L_0(R_0 + K))}{KK_d}\right).$$

To fairly compare this result to that for the "double-negative" pathway, we further assume that $R_0 \gg K$, obtaining

$$\lambda_S \approx \lambda_L \ln\left(\frac{(e-1)L_0 R_0}{KK_d}\right). \quad \text{(B.14)}$$

Given Eq. B.11, the results in Eqs. B.13-14 show that in the "double-positive" pathway, signaling gradient amplitude primarily depends on the receptor production rate only, and decay length depends on the product of ligand and receptor production rates. Notably, the assumption of $L_0 >> K_d$ causes the signal to be saturated with respect to L_0, such that changes in L_0 cannot be sensed. In summary, the “double-negative” logic of the HH pathway is sufficient to generate the ratiometric behavior, and this behavior is unique to the “double-negative” pathway architecture.

C. GLIR-only open loop model of HH spatio-temporal dynamics

C.1. Cell-autonomous HH signaling model

In the HH pathway, in the absence of ligand, PTCH actively suppresses Smoothened, leading to the preferential processing of full-length GLI proteins into its transcriptional repressor form, GLIR. Ligand binding inactivates PTCH, relieving PTCH’s inhibition of Smoothened. Activated Smoothened biases the processing of full-length GLI into its transcriptional activator form, GLIA. Because GLIA and GLIR share the same DNA-binding domain, they bind to the same binding sites (GBS) to influence transcription.

Because we are interested in the input-output relationship describing the dependence of gene expression (which we refer to as “signaling activity”) on ligand, we sought a simple model describing this relationship. We found that we could capture the temporal dynamics of signaling activity in response to bath application of ligand (Fig. S5B) with a model that includes only the receptor PTCH, the PTCH-HH complex, the repressor GLIR, and reporter gene expression (Fig. S5A). In this model, free PTCH promotes production of GLIR. When PTCH binds to HH, GLIR production ceases, and GLIR levels fall as GLIR is degraded. As GLIR levels fall below the repression threshold K_R, gene expression increases. The time needed for GLIR levels to fall before gene expression substantially increases creates the time delay observed in the “0D” bath application experiments.

The signaling intermediate *R* is included to produce the stereotypical time delay consistently observed in our experiments (Figs. S3D, S13C); a model in which *P* directly represses *S* production can recapitulate the steady-state dose response curve but not the time delay (results not shown). Using GLIR dilution to create a time delay is consistent with experimental work suggesting that levels of repressive GLI protein could control the dynamics of pathway activation *(47)*.

We find that a more complex model explicitly describing full-length GLI and both GLIA and GLIR (Fig. S6A) produces similar results as the GLIR-only model (Fig. S6). To focus on the role of feedback rather than the details of signal transduction, we use the simpler, GLIR-only model (Fig. S5A) throughout the main text and figures.

The cell-autonomous ("0D") GLIR-only model (Fig. S5A) includes four dynamical variables: free receptor PTCH (*P*), HH-PTCH complex (*C*), GLIR repressor (*R*), and the signaling reporter (*S*). Free HH (*H*) is assumed to be constant, as HH is applied in a large bath of media that should create a large reservoir of ligand. We made the following assumptions:

(1) *P* promotes production of *R*, which inhibits signaling. *H* binds to *P* to create complex *C*; this depletes *P*, which in turn results in reduced production of *R*. *R* levels fall as *R* is degraded, resulting in de-repression of signaling.

(2) The signaling-controlled promoter (*S*) has a GLI-independent basal activity ($\alpha_{GBS,0}$) and GLI-dependent activity ($\alpha_{GBS} * \varphi_R$), with α_{GBS} being the maximum GLI-regulated activity and φ_R being the degree of activation ranging from 0 to 1. φ_R is negatively controlled by GLIR. Specifically, φ_R is given by

$$\varphi_R = \frac{{K_R}^{n_R}}{{K_R}^{n_R} + R^{n_R}}. \tag{C.1}$$

With these assumptions, we obtain four ordinary differential equations describing the system

$$\frac{dP}{dt} = \alpha_{PTC} - \gamma_P P - k_{on} HP + k_{off} C \tag{C.2}$$

$$\frac{dC}{dt} = k_{on} HP - k_{off} C - \gamma_C C \tag{C.3}$$

$$\frac{dR}{dt} = \alpha_R \frac{P^{n_P}}{{K_P}^{n_P} + P^{n_P}} - \gamma_R R \tag{C.4}$$

$$\frac{dS}{dt} = \alpha_{GBS,0} + \alpha_{GBS} \varphi_R. \tag{C.5}$$

Parameter values were determined by fitting this model to the 0D SHH dose response data (Fig. S5B, Table S2; see materials and methods).

C.2. Addition of spatial dynamics to the model

To model the spatial aspects of HH signaling, we started with the 0D system (Eqs. C.1-5), adding *H* as a dynamical variable and making all species a function of space as well as time. *H* is the only mobile species, diffusing with diffusion constant *D*, and its dynamics are described by

$$\frac{\partial H}{\partial t} = D \frac{\partial^2 H}{\partial x^2} - \gamma_H H - k_{on} HP + k_{off} C. \tag{C.6}$$

To describe the quasi-1D gradients examined experimentally (Fig. 2B-C), we model the system in one spatial dimension. We thus obtain a system of five coupled partial differential equations (Eqs. C.2-6), with *P*, *C*, *R* and *S* modeled using the same equations as for the 0D system.

The boundary conditions are a fixed influx α_{HH} of *H* at the sender-receiver boundary on the left-hand side and a zero-boundary condition at the other end of the receiver field:

$$\left.\frac{\partial H}{\partial x}\right|_{x=0} = -\alpha_{HH}/D \tag{C.7}$$

$$H(x = L) = 0 \tag{C.8}$$

where *L* is the width of the receiver domain. The added parameters (*D*, γ_H, and α_{HH}) were determined by fitting to the observed gradient formation dynamics in the open loop system for three different α_{HH}, all at 1x α_{PTC} (Fig. S5C, Table S2), with the cell-autonomous parameters from Eqs. C.1-5 fixed to those derived from the 0D fit. We also included a multiplicative factor *m* relating the experimental 0D and 1D data signaling amplitudes. Because *m* is a phenomenological factor unrelated to our mechanistic model, we do not include it in these equations). See the "Parameter fitting" section in materials and methods.

D. *Feedback models based on the GLIR-only model*

D.1. PTCH feedback

To simulate PTCH feedback, we introduce a GLIR-dependent production term for PTCH, while retaining its constitutive production term α_{PTC}. The new term includes a maximum feedback-dependent production rate, $\beta^*\alpha_{PTC}$, where β describes the maximum ratio of feedback-regulated production to constitutive production. Notably, β is the only new parameter introduced (boldfaced below) to describe feedback. Feedback-regulated production of *P* is inhibited by *R* according to same Hill-like function, $\varphi_R(R)$ (Eq. C.1), through which *R* inhibits production of *S*. The boundary conditions are the same as for the open loop model (Eqs. C.7-C.8).

$$\frac{\partial H}{\partial t} = D\frac{\partial^2 H}{\partial x^2} - \gamma_H H - k_{on}HP + k_{off}C \tag{D.1}$$

$$\frac{\partial P}{\partial t} = \alpha_{PTC} + \boldsymbol{\beta}\alpha_{PTC}\varphi_R - \gamma_P P - k_{on}HP + k_{off}C \tag{D.2}$$

$$\frac{\partial C}{\partial t} = k_{on}HP - k_{off}C - \gamma_C C \tag{D.3}$$

$$\frac{\partial R}{\partial t} = \alpha_R \frac{P^{n_P}}{{K_P}^{n_P} + P^{n_P}} - \gamma_R R \tag{D.4}$$

$$\frac{\partial S}{\partial t} = \alpha_{GBS,0} + \alpha_{GBS}\varphi_R \tag{D.5}$$

D.2. Models for alternative feedback architectures

In Fig. 3 and Figs. S7-9, we compare PTCH feedback to alternative negative feedback architectures that omit certain molecular features of the PTCH feedback (Figs. 3A, S7A). Specifically, we examined the behavior of feedbacks lacking either extracellular activity (yielding purely intracellular feedback) or intracellular activity (yielding purely extracellular feedback), as well as feedback that implements both activities through distinct proteins (uncoupled feedback). Intracellular (IC) feedback operates through production of a species *I* that inhibits signaling intracellularly but does not bind to HH. Extracellular (EC) feedback operates through production of a species *E* that binds to HH but does not influence GLIR production. Uncoupled feedback features feedback-dependent production of both *I* and *E*. In all three models, PTCH is produced constitutively (as in the open loop model, Eqs. C.1 - C.6); PTCH production is required even in the IC, EC, and uncoupled models because PTCH is the only species capable of transducing extracellular HH concentration to intracellular signal activity.

To facilitate a direct and well-controlled comparison between these models, we assume that all feedback species have the same biochemical properties as PTCH (i.e., the same rate constants or parameters for production, degradation, binding and unbinding to HH, and regulation of GLIR) except for the specific activity it lacks by design (GLIR regulation for *E*, HH binding/unbinding for *I*). *E* and *I* are produced according to the same GLIR-inhibited, Hill-like function φ_R (Eq. C.1) that controls *P* production, except that the scaling factors β_E and β_I need not be equal to β.

The equations describing IC, EC, and uncoupled feedbacks are described below. The only free parameters – those not determined by the open loop fit – are β_E and β_I and are **boldfaced**. The boundary conditions are the same as for the open loop model (Eqs. C.7 – 8).

IC model

$$\frac{\partial H}{\partial t} = D\frac{\partial^2 H}{\partial x^2} - \gamma_H H - k_{on}HP + k_{off}C \tag{D.6}$$

$$\frac{\partial P}{\partial t} = \alpha_{PTC} - \gamma_P P - k_{on}HP + k_{off}C \tag{D.7}$$

$$\frac{\partial C}{\partial t} = k_{on}HP - k_{off}C - \gamma_C C \tag{D.8}$$

$$\frac{\partial I}{\partial t} = \boldsymbol{\beta_I}\alpha_{PTC}\varphi_R - \gamma_P I \tag{D.9}$$

$$\frac{\partial R}{\partial t} = \alpha_R \frac{(P+I)^{n_P}}{{K_P}^{n_P} + (P+I)^{n_P}} - \gamma_R R \tag{D.10}$$

$$\frac{\partial S}{\partial t} = \alpha_{GBS,0} + \alpha_{GBS}\varphi_R \tag{D.11}$$

EC model

$$\frac{\partial H}{\partial t} = D\frac{\partial^2 H}{\partial x^2} - \gamma_H H - k_{on}H(P+E) + k_{off}(C+C_E) \tag{D.12}$$

$$\frac{\partial P}{\partial t} = \alpha_{PTC} - \gamma_P P - k_{on}HP + k_{off}C \tag{D.13}$$

$$\frac{\partial E}{\partial t} = \boldsymbol{\beta_E}\alpha_{PTC}\varphi_R - \gamma_P E - k_{on}HE + k_{off}C_E \tag{D.14}$$

$$\frac{\partial C}{\partial t} = k_{on}HP - k_{off}C - \gamma_C C \tag{D.15}$$

$$\frac{\partial C_E}{\partial t} = k_{on}HE - k_{off}C_E - \gamma_C C_E \tag{D.16}$$

$$\frac{\partial R}{\partial t} = \alpha_R \frac{P^{n_P}}{{K_P}^{n_P} + P^{n_P}} - \gamma_R R \tag{D.17}$$

$$\frac{\partial S}{\partial t} = \alpha_{GBS,0} + \alpha_{GBS}\varphi_R \tag{D.18}$$

Uncoupled IC+EC model

$$\frac{\partial H}{\partial t} = D\frac{\partial^2 H}{\partial x^2} - \gamma_H H - k_{on}H(P+E) + k_{off}(C+C_E) \quad \text{(D.19)}$$

$$\frac{\partial P}{\partial t} = \alpha_{PTC} - \gamma_P P - k_{on}HP + k_{off}C \quad \text{(D.20)}$$

$$\frac{\partial E}{\partial t} = \boldsymbol{\beta_E}\alpha_{PTC}\varphi_R - \gamma_P E - k_{on}HE + k_{off}C_E \quad \text{(D.21)}$$

$$\frac{\partial C}{\partial t} = k_{on}HP - k_{off}C - \gamma_C C \quad \text{(D.22)}$$

$$\frac{\partial C_E}{\partial t} = k_{on}HE - k_{off}C_E - \gamma_C C_E \quad \text{(D.23)}$$

$$\frac{\partial I}{\partial t} = \boldsymbol{\beta_I}\alpha_{PTC}\varphi_R - \gamma_P I \quad \text{(D.24)}$$

$$\frac{\partial R}{\partial t} = \alpha_R\frac{(P+I)^{n_P}}{{K_P}^{n_P} + (P+I)^{n_P}} - \gamma_R R \quad \text{(D.25)}$$

$$\frac{\partial S}{\partial t} = \alpha_{GBS,0} + \alpha_{GBS}\varphi_R \quad \text{(D.26)}$$

Coupled, non-switching model

We also considered a model in which feedback produces a protein *Y* with physically-linked (coupled) intracellular and extracellular functionalities, but in which intracellular function does not depend on ligand-binding state (Fig. S9D).

$$\frac{\partial H}{\partial t} = D\frac{\partial^2 H}{\partial x^2} - \gamma_H H - k_{on}H(P+Y) + k_{off}(C+C_Y) \quad \text{(D.27)}$$

$$\frac{\partial P}{\partial t} = \alpha_{PTC} - \gamma_P P - k_{on}HP + k_{off}C \quad \text{(D.28)}$$

$$\frac{\partial Y}{\partial t} = \boldsymbol{\beta_Y}\alpha_{PTC}\varphi_R - \gamma_P Y - k_{on}HY + k_{off}C_Y \quad \text{(D.29)}$$

$$\frac{\partial C}{\partial t} = k_{on}HP - k_{off}C - \gamma_C C \quad \text{(D.30)}$$

$$\frac{\partial C_Y}{\partial t} = k_{on}HY - k_{off}C_Y - \gamma_C C_Y \quad \text{(D.31)}$$

$$\frac{\partial R}{\partial t} = \alpha_R\frac{(P+Y)^{n_P}}{{K_P}^{n_P} + (P+Y)^{n_P}} - \gamma_R R \quad \text{(D.32)}$$

$$\frac{\partial S}{\partial t} = \alpha_{GBS,0} + \alpha_{GBS}\varphi_R \quad \text{(D.33)}$$

E. GLIA + GLIR models to simulate open loop and various closed loop gradients

In most biological contexts, both GLI Repressor (*R*) and Activator (*A*) are produced from full-length GLI protein (*F*), and they compete for the same binding sites on DNA *(4, 18, 39, 48).* Therefore, we expanded our GLIR-only model to include this additional detail, and then compared different feedback architectures in the context of this expanded model. In the new set of GLIA+GLIR models (Fig. S10A), we made the following assumptions:

(1) Free PTCH (*P*) regulates the production rate of *A*, but not *R*. R is produced constitutively from F.

(2) The signaling-controlled promoter (*S*) has a GLI-independent basal activity ($\alpha_{GBS,0}$) and GLI-dependent activity ($\alpha_{GBS} * \varphi_{AR}$), with α_{GBS} being the maximum possible GLI-dependent activity and φ_{AR} being the degree of activation ranging from 0 to 1. φ_{AR} is controlled by two GLI binding sites for simplicity and consistency with published literature (*18*, *48*). φ_{AR} is non-zero only when at least one of the sites is bound by GLIA and neither site is bound by GLIR. When both sites are bound by GLIA, the promoter produces twice as many transcripts as when only a single site is bound by GLIA. With these assumptions, we obtain

$$\varphi_{AR} = \frac{A^2 + K_{gli}A}{A^2 + 2K_{gli}A + 2K_{gli}R + 2AR + R^2 + K_{gli}^2} \tag{E.1}$$

(3) φ_{AR} controls the feedback loops, in lieu of φ_R.

The GLIA+GLIR open loop model has 7 species:

- *H*, *P*, *C* and *S* are modeled identically to the GLIR-only open loop model (Eqs. C.2-3, C.5-6), except that φ_R is replaced with φ_{AR} (Eq. E.1).
- The GLI species are simulated as follows:

$$\frac{\partial F}{\partial t} = \alpha_F - \left(a_A \frac{{K_P}^{n_P}}{{K_P}^{n_P} + P^{n_P}} + a_R + \gamma_F \right) F \tag{E.2}$$

$$\frac{\partial A}{\partial t} = a_A \frac{{K_P}^{n_P}}{{K_P}^{n_P} + P^{n_P}} F - \gamma_A A \tag{E.3}$$

$$\frac{\partial R}{\partial t} = \alpha_R F - \gamma_R R \tag{E.4}$$

The GLIA+GLIR PTCH feedback model has 7 species:

- *H*, *P*, *C* and *S* are modeled identically to the GLIR-only PTCH feedback model (Eqs. D.1-3, 5), except that φ_R is replaced with φ_{AR} (Eq. E.1).
- *F*, *A*, and *R* are modeled identically to the GLIA+GLIR open loop model (Eqs. E.2-4).

The GLIA+GLIR IC feedback model has 8 species:

- *H*, *P*, C, *I* and *S* are identical to the GLIR-only IC feedback model (Eqs. D.6-9, 11), except that φ_R is replaced with φ_{AR} (Eq. E.1).
- *F*, *A*, and *R* are modeled identically to the GLIA+GLIR open loop model (Eqs. E.2-4).

The GLIA+GLIR EC feedback model has 9 species:

- *H*, *P*, *C*, *E*, C_E and *S* are identical to the GLIR-only EC feedback model (Eqs. D.12-16, 18), except that φ_R is replaced with φ_{AR} (Eq. E.1).
- *F*, *A*, and *R* are identical to the GLIA+GLIR open loop model (Eqs. E.2-4).

The GLIA+GLIR uncoupled feedback model has 10 species:

- *H*, *P*, *C*, *E*, C_E, *I* and *S* are identical to the GLIR-only uncoupled feedback model (Eqs. D.19-24, 26), except that φ_R is replaced with φ_{AR} (Eq. E.1).
- *F*, *A*, and *R* are identical to the GLIA+GLIR open loop model (Eqs. E.2-4).

The open loop GLIA+GLIR model was fit to the experimental data using the same procedure as described for the GLIR-only model (Fig. S5B-D). This leaves the feedback strengths as the only tunable parameters. Simulations were performed using the same boundary conditions as in the GLIR-only model (Eqns. C.7-C.8). In the resulting model output, GLIA levels exceed GLIR levels proximal to the source, while GLIR levels exceed GLIA levels in distal regions, showing that in this parameter regime both forms of GLI play a role (Fig. S6D). This new set of models recapitulates the key conclusions of the GLIR-only models, including the ratiometric behavior of the open loop system and the robustness properties of different closed loop circuits (Figs. S6E, S10). These results demonstrate the separability of two levels of regulation: ligand-receptor interactions and intracellular signal transduction through GLI. The GLI-level regulation represents a module that processes input from unliganded PTCH (and, when present, *I*) and converts it to a target gene expression level. This module can be implemented in different ways (i.e., through GLIR alone or a combination of GLIA and GLIR) that produce the empirically-observed dose response, and therefore preserves the effects of receptor-level feedback.

F. GLI2+GLI3 models with upregulation of GLI2 (positive feedback)

Unstimulated NIH3T3 cells predominantly express two GLI proteins, GLI2 and GLI3, at a similar mRNA level (Table S1). GLI2 acts mostly as a transcription activator, whereas GLI3 is both an activator and repressor. SHH pathway activation induces a 2-fold upregulation of GLI2, but not GLI3, and thus provides a positive feedback loop. To take these details into consideration, we further expanded the GLIA+GLIR models to explicitly represent full-length GLI2 (F_2) and GLI3 (F_3). In this new set of models, we made the following assumptions:

(1) Both F_2 and F_3 are produced and degraded at the same basal rates (rate constants α_F and γ_F, respectively).
(2) Both F_2 and F_3 are processed into GLIA at the same maximum rate (α_A) with the same dependence on free PTCH (*P*). The GLIAs derived from F_2 or F_3 are indistinguishable.
(3) Both F_2 and F_3 are processed into GLIR at constant rates (α_{R2} and α_{R3}) with α_{R2} being much smaller than α_{R3}, pushing GLI2 to the activator form. The GLIRs derived from F_2 or F_3 are indistinguishable.
(4) F_2 production also depends on the signal, forming a positive feedback loop (β_{FL} representing the strength of this feedback).

The GLI2+GLI3 open loop model (Fig. S11A) with upregulation of GLI2 has 8 species:

- *H, P, C* and *S* are identical to the GLIR-only open loop model (Eqs. C2-3, C5-6), except that φ_R is replaced with φ_{AR} (Eq. E.1).
- The GLI species are simulated as follows.

$$\frac{\partial F_2}{\partial t} = \alpha_F(1 + \beta_{FL}\varphi_{AR}) - \left(a_A \frac{{K_P}^{n_P}}{{K_P}^{n_P} + P^{n_P}} + a_{R2} + \gamma_F\right) F_2 \tag{F.1}$$

$$\frac{\partial F_3}{\partial t} = \alpha_F - \left(a_A \frac{{K_P}^{n_P}}{{K_P}^{n_P} + P^{n_P}} + a_{R3} + \gamma_F\right) F_3 \tag{F.2}$$

$$\frac{\partial A}{\partial t} = a_A \frac{{K_P}^{n_P}}{{K_P}^{n_P} + P^{n_P}} (F_2 + F_3) - \gamma_A A \tag{F.3}$$

$$\frac{\partial R}{\partial t} = \alpha_{R2} F_2 + \alpha_{R3} F_3 - \gamma_R R \tag{F.4}$$

The GLI2+GLI3 PTCH feedback model with upregulation of GLI2 has 8 species:

- *H, P, C* and *S* are identical to the GLIR-only PTCH feedback model (Eqs. D.1-3, D.5), except that φ_R is replaced with φ_{AR} (Eq. E.1).
- F_2, F_3, *A* and *R* are modeled with Eqs. F.1-4.

The GLI2+GLI3 IC feedback model with upregulation of GLI2 has 9 species:

- *H, P, C* and *S* are identical to the GLIR-only PTCH feedback model (Eqs. D.6-9, D.11), except that φ_R is replaced with φ_{AR} (Eq. E.1).
- F_2, F_3, *A* and *R* are modeled with Eqs. F.1-4.

The GLI2+GLI3 EC feedback model with upregulation of GLI2 has 10 species:

- *H, P, C, E,* C_E and *S* are identical to the GLIR-only EC feedback model (Eqs. D.12-16, D.18), except that φ_R is replaced with φ_{AR} (Eq. E.1).
- F_2, F_3, *A* and *R* are modeled with Eqs. F.1-4.

The GLI2+GLI3 uncoupled feedback model with upregulation of GLI2 has 11 species:

- *H, P, C, E,* C_E, *I* and *S* are identical to the GLIR-only uncoupled feedback model (Eqs. D.19-24, D.26), except that φ_R is replaced with φ_{AR} (Eq. E.1).
- F_2, F_3, *A* and *R* are modeled with Eqs. F.1-4.

G. *A GLIA + GLIR model with downregulation of full-length GLIFL to create temporal adaptation*

In some developmental contexts, SHH signaling activity exhibits complete temporal adaptation, primarily due to the downregulation of full-length GLI production (*18*). To compare different feedback models under adaptive dynamics, we simulated all the models in Section E using the same parameters, except allowing the production rate of full-length GLI, α_F, to be time-dependent (Fig. S12A-B). Computationally, $\alpha_F(t)$ is a piece-wise linear function, with the transition timepoints ($t_{downreg}$ = 30 h and 2.5*$t_{downreg}$ = 75 h) chosen to match the observed signaling dynamics in mouse neural tubes (*10*).

$$\alpha_F(t) = \begin{cases} \alpha_F & when\ t \le t_{downreg} \\ \alpha_F\left(2.5t_{downreg} - t\right) \Big/ 1.5t_{downreg} & when\ t_{downreg} \le t \le 2.5t_{downreg} \\ 0 & when\ t > 2.5t_{downreg} \end{cases} \quad \text{(G.1)}$$

All models were run for 96 hours. Complete adaptation was observed after 80 hrs. Because the steady state activity is zero for all models and positions, we analyzed the gradient amplitude, lengthscale and shape of *S* (the integrated signaling activity) at 96 hrs (Fig. S12D).

H. Modeling methods and metrics

For Fig. 2 and figs. S5-6 and S12, the lengthscale λ is defined in terms of the integrated signal $S(t,x)$. t_{end} is the last timepoint of the simulation.

$$\lambda \equiv max\left\{x \;\middle|\; S(t_{end}, x) \ge \frac{1}{e} * S(t_{end}, 1)\right\}) \quad \text{(H.1)}$$

For Fig. 3 and figs. S7-11, the lengthscale λ is defined in terms of the instantaneous signal at steady state, $\frac{\partial S(t_{end},x)}{\partial t}$, where t_{end} is the last timepoint of the simulation, which runs until the system is at steady state (defined in Eq. H.5).

$$\lambda \equiv max\left\{x \;\middle|\; \frac{\partial S(t_{end},x)}{\partial t} \ge \frac{1}{e} * \frac{\partial S(t_{end},1)}{\partial t}\right\}) \quad \text{(H.2)}$$

For figs. S5-6 and 12, the amplitude *A* is defined in terms of the background-subtracted, integrated signal at steady state $S(t_{end}, x)$,

$$A \equiv\ S(t_{end}, 1) -\ S(t_{end}, 1000). \quad \text{(H.3)}$$

For Fig. 3 and figs. S7-11, the amplitude *A* is defined in terms of the background-subtracted, instantaneous signal at steady-state, $\frac{\partial S(t_{end},x)}{\partial t}$,

$$A \equiv \frac{\partial S(t_{end}, 1)}{\partial t} - \frac{\partial S(t_{end}, 1000)}{\partial t}. \quad \text{(H.4)}$$

For the purposes of determining whether the system as a whole has reached steady state in a simulation, the steady state is defined as the first timepoint t_i at which, for all species *G* (except *S*) and for all *x*,

$$\left|\frac{G(t_i + \delta, x) - G(t_i, x)}{G(t_i, x)}\right| < 10^{-3} \text{ for } 0 < \delta \leq 4.5\ h \quad \text{(H.5)}$$

The time τ for a quantity *G* (e.g., $\partial S/\partial t$) to reach steady state at x_{50} (where x_{50} is the distance at which G equals 50% of its own steady-state maximum) is defined as

$$\tau \equiv min\left\{t \,\middle|\, abs\left(\frac{G(t, x_{50}) - G(t_{end}, x_{50})}{G(t_{end}, x_{50})}\right) \leq 0.10\right\}. \quad \text{(H.6)}$$

The sensitivity $\sigma_{y,\alpha_{HH}}$ of a metric *y* to a change in α_{HH} is defined for a 2-fold change in α_{HH}:

$$\sigma_{y,\alpha_{HH}} \equiv \frac{\partial \ln y}{\partial \ln \alpha_{HH}} \approx \frac{(y_{2*\alpha_{HH}} - y_{\alpha_{HH}})/y_{\alpha_{HH}}}{(2 * \alpha_{HH} - \alpha_{HH})/\alpha_{HH}} = \frac{(y_{2*\alpha_{HH}} - y_{\alpha_{HH}})}{y_{\alpha_{HH}}} \quad \text{(H.7)}$$

The shape factor θ is defined as the length L_2 of the second third of the gradient (i.e., the distance over which $\partial S/\partial t$ decreases from ⅔ to ⅓ of the gradient amplitude) divided by the length L_1 of the first third of the gradient at steady state, or

$$\theta = \frac{L_2}{L_1}. \quad \text{(H.8)}$$

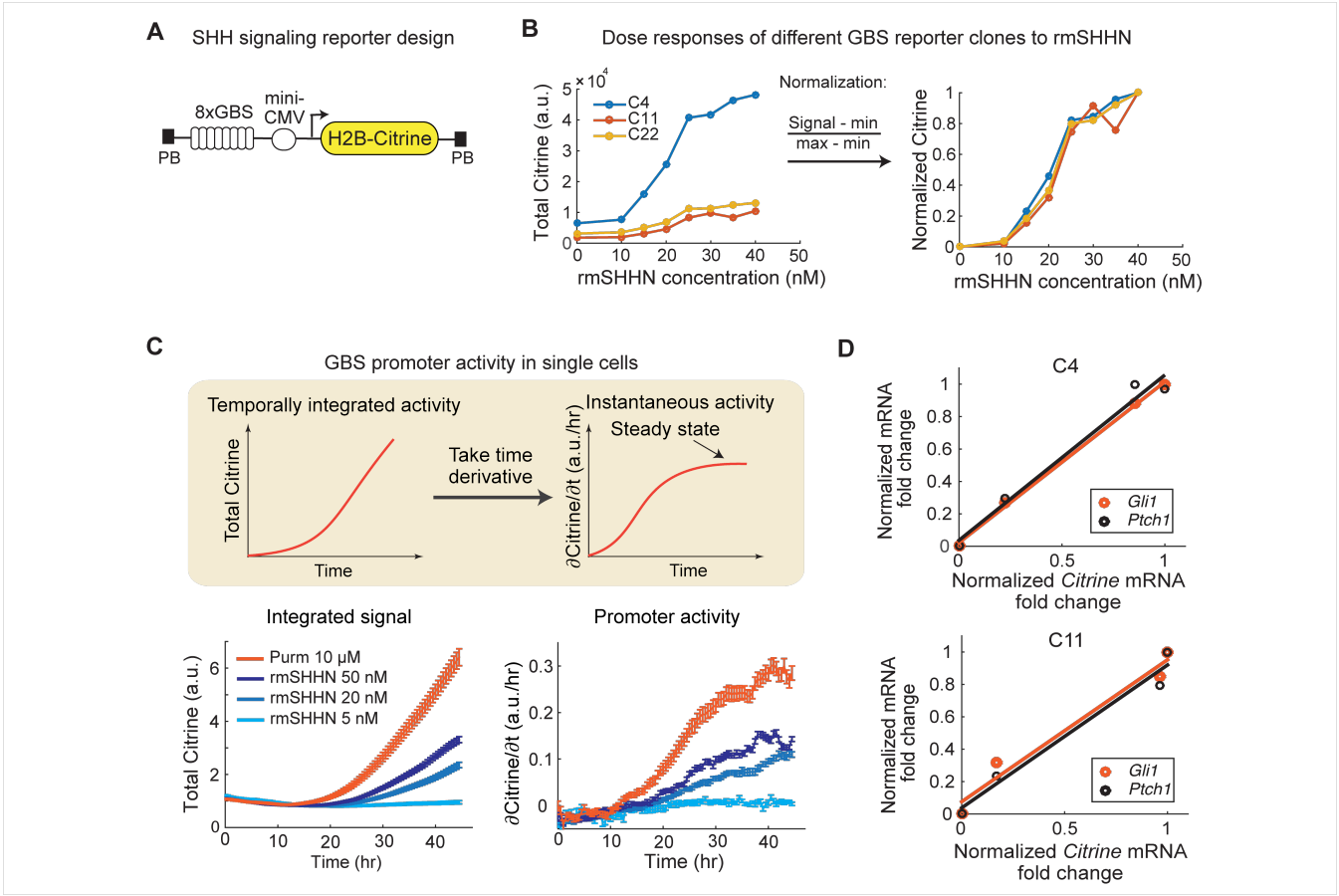

Fig. S1. Characterization of the GBS reporter for SHH signaling activity.

(A) The fluorescence reporter construct contains 8 tandem copies of GLI binding sequences (GBS), a minimal CMV promoter (miniCMV) and Citrine fluorescence protein fused to Histone H2B, all cloned into a PiggyBac vector (PB). **(B)** Dose response to rmSHHN (recombinant mouse SHH N-terminal peptide) treatment after 48 hrs in three representative clonal reporter cell lines (C4, C11 and C22, all in wild-type NIH3T3 background), measured by the population mean of Citrine intensity by flow cytometry. Different clones have similar dose response profiles (normalized curves, *right*), with variations in the absolute amplitude (*left*), potentially due to different copy numbers of the integrated reporter construct. min, basal level of Citrine without rmSHHN stimulation; max, maximum Citrine at saturating levels of rmSHHN. **(C)** Signaling dynamics in individual reporter cells by single-cell time-lapse imaging (mean ± s.e.m. for 50-100 cells each). H2B concentrates and stabilizes the Citrine fluorescent reporter in the nucleus, leading to a negligible Citrine degradation rate. Therefore, total Citrine represents temporally integrated signal, and its time derivative represents the promoter activity of the reporter, which is directly controlled by the instantaneous signaling activity in the cell (*schematic*, see Material and Methods "Calculation of instantaneous signaling activity" section for detailed explanation). SHH and Purmorphamine (Purm) activate the downstream pathway through different mechanisms, with Purm directly activating SMO downstream of the SHH receptor PTCH. Purm stimulation leads to a higher promoter activity, indicating that the saturating concentration of rmSHHN (50 nM) does not saturate the promoter of the reporter. **(D)** *Citrine* mRNA fold change linearly correlates with endogenous targets (*Gli1* and *Ptch1*) of the SHH pathway in the C4 and C11 reporter cell lines. Reporter cells were stimulated with various rmSHHN concentrations for 48 hrs and analyzed by qRT-PCR. To represent *Gli1* and *Ptch1* fold changes on the same scale, results were normalized with the following calculation: (fold change - min)/(max-min), with min representing 0 nM rmSHHN and max representing the highest rmSHHN concentration. We chose C4 for all subsequent cell line engineering and gradient experiments.

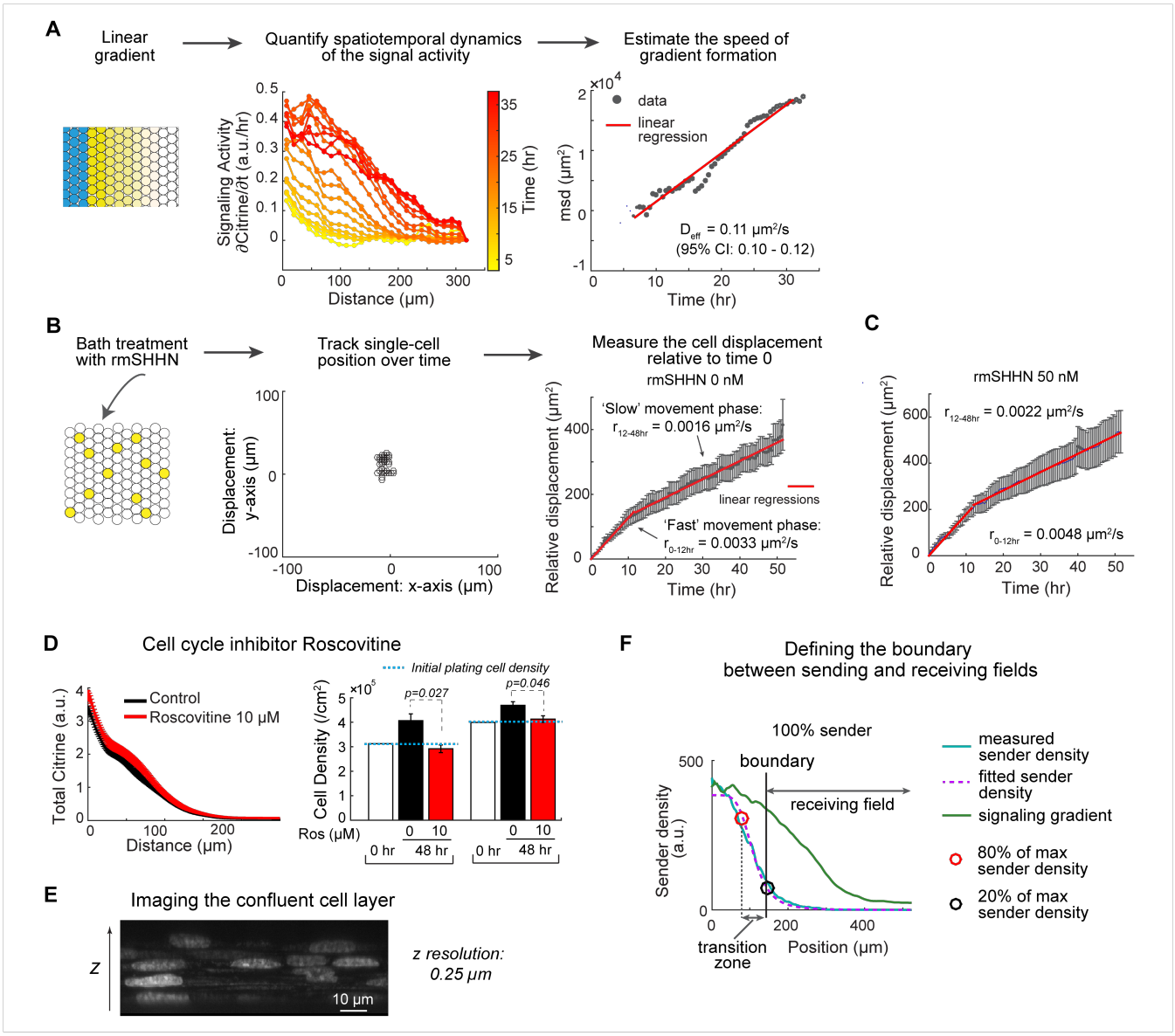

Fig. S2. Quantifying the effects of cell migration, proliferation and overlap on gradient formation.
(A) Estimation of the effective diffusion constant for signaling gradient formation (D_{eff}). The spatiotemporal dynamics of signaling gradients were recorded by time-lapse imaging. The signaling activity, approximated by the rate of Citrine fluorescent reporter accumulation, which was calculated by taking the time derivative of total Citrine fluorescence. D_{eff} is given by linearly regressing the mean squared displacement (msd) of signaling activity on time (see Materials and Methods for details). **(B)** Estimation of the speed of cell movement. Reporter cells (yellow) were diluted in an excess of 'dark' wild-type 3T3 cells, with a total cell density comparable to that in the spatial gradients. Cells were treated with rmSHHN, and Citrine fluorescence was monitored by time-lapse imaging. The positions of individual reporter cells were tracked, and the spatial displacement of each cell in a single dimension relative to its initial position was plotted as a function of time. Plots of the squared displacement versus time are biphasic, with faster cell movement during the first 12 hrs and slower movement later. This behavior was quantified with a piecewise linear regression. The speed of cell movement in both phases is less than 10% of the speed of gradient formation, suggesting that cell movement plays an insignificant role in gradient formation. Data (*gray*) show mean ± s.d. (n=303). (see Materials and Methods for more details). **(C)** SHH concentration does not have major effects on the speed of cell movement (*top*, n=288; *bottom*, n=338). **(D)** Inhibition of cell division with Roscovitine does not significantly affect gradient formation *(left)*. *Right*: The rate of cell division depends on the initial plating density (*white bars*), and division can be completely inhibited

by 10 μM Roscovitine (mean ± s.d., student t-test). **(E)** Confocal microscopy shows that NIH3T3 cells cultured at confluency for 48 h form a multi-layered structure. **(F)** Defining the boundary between the sending and receiving fields. The sender density profile (*cyan*) was quantified by summing the number of mTurquoise2-positive pixels along each column, then fitting the sum to an inverse Hill function (*magenta dotted line*). Throughout the paper, the sender-receiver boundary is defined as the position at which the sender density drops to 20% of the maximum density (*black solid line*), to minimize the number of senders in the receiver zone. The region in which the sender density drops from 80% to 20% of the maximum density (*red* and *black circles*, respectively) represents a "transition zone". The qualitative results in the paper do not depend on the exact value of the boundary threshold parameter, as Citrine levels change minimally within the transition zone.

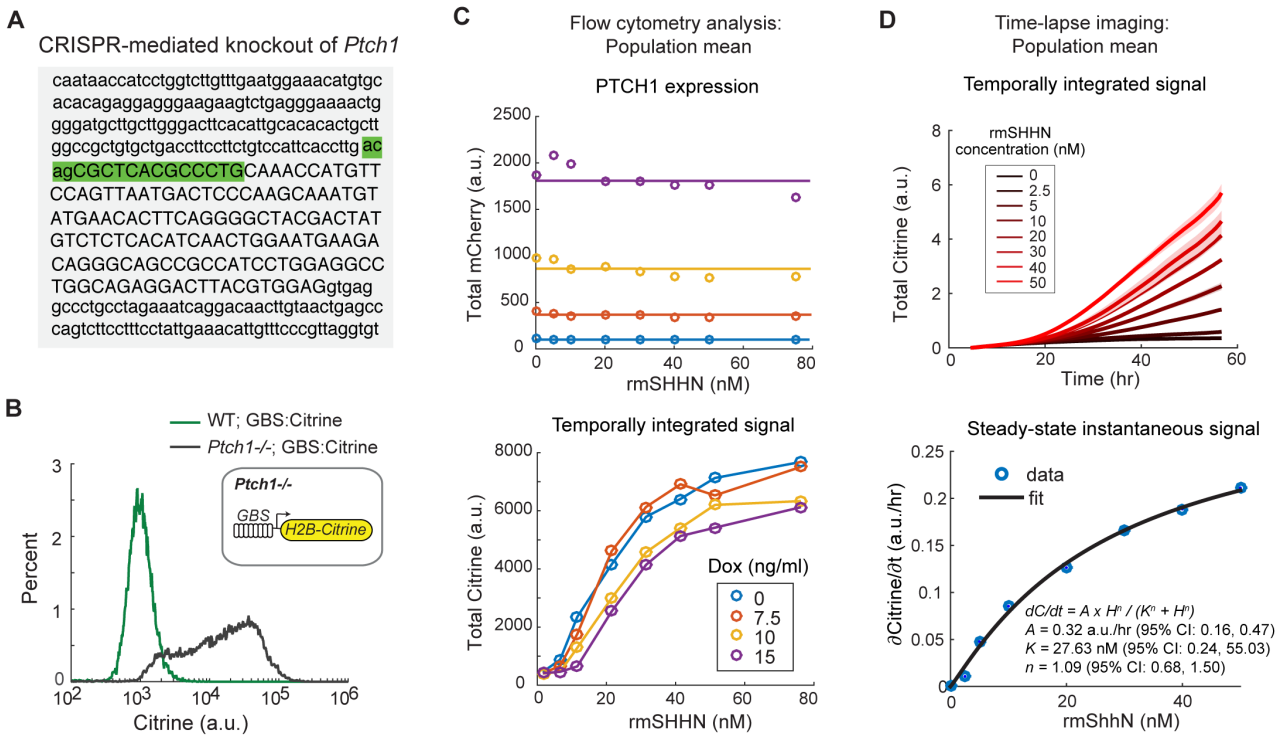

Fig. S3. Construction and characterization of open loop receiver cells (as shown in Fig. 2A)

(A) CRISPR-mediated deletion in both alleles of *Ptch1* in the genome of SHH reporter cells (homozygous with the same mutation). Lower-case letters, intron sequences; uppercase letters, exon sequences; green highlights the deleted sequence. **(B)** *Ptch1* homozygous deletion activates SHH signal reporter in the receiver cells in the absence of SHH. Flow cytometry 1 day after cells reached 100% confluency. **(C)** Flow cytometry analysis of open loop receiver cells (Fig. 2A) after 72 hrs of Dox and/or rmSHHN induction. Notice that basal leaky expression of PTCH1 from the *TRE* promoter (Dox 0 ng/ml) was sufficient to suppress auto-activation in *Ptch1*$^{-/-}$ cells. Additional PTCH1 expression can be tuned by titrating Dox concentration (ng/ml), as reported by the mCherry level (*top*). Increasing PTCH1 level reduces cell response to bath treatment with rmSHHN (*bottom*). **(D)** Time-lapse imaging of the signal response dynamics under different rmSHHN concentrations (mean ± s.e.m., n=5). *Top*: Total Citrine represents temporally integrated signal; *Bottom*: the mean instantaneous signaling activity between 35-50 hr (*blue circles*) can be fit to a Hill-like dose titration curve (*black line*), with the fitted equation, coefficient values and their confidence intervals displayed.

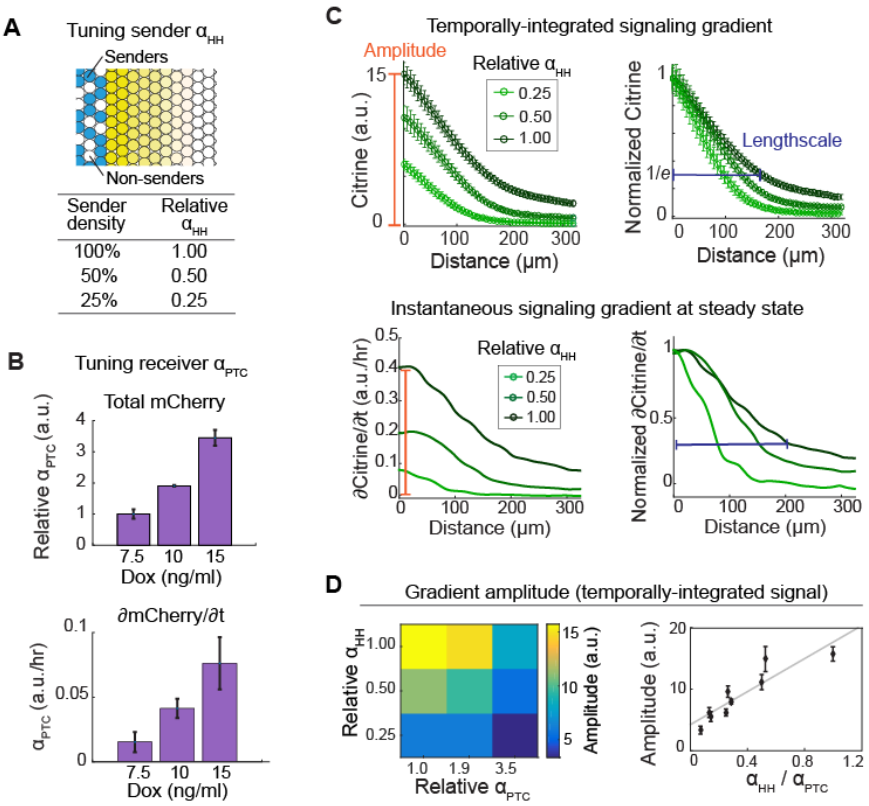

Fig. S4. Characterizing the dependence of open loop signaling gradient features on α_{HH} and α_{PTC} (see also Fig. 2).

Gradients were reconstituted in the linear geometry with open loop receivers. **(A)** Senders and dark (unlabeled) wild-type NIH3T3 cells were mixed at different ratios to tune the ligand production rate (α_{HH}); this sets the "relative α_{HH}" value, defined as the ratio between the effective rate of ligand secretion at a given dilution to that at 100% senders. **(B)** Quantification of PTCH1 expression by measuring the total H2B-mCherry fluorescence (*top*) or the promoter activity of mCherry (*bottom*), mean ± s.d. (n=20). **(C)** Increasing α_{HH} increases gradient amplitude (*orange bar*) and lengthscale (*blue bar*). Amplitude is defined as the signaling activity in the cell closest to the boundary. Lengthscale is measured by the distance where the signaling gradient drops below 1/*e* of its own amplitude. Gradients were quantified by either the time-integrated signal activity (*top plots*) or instantaneous signal activity (∂Citrine/∂t) at steady state (*bottom plots*). Representative gradient images are shown in Fig. 2E. **(D)** Gradient amplitude ratiometrically depends on the ligand and receptor production rates (α_{HH} and α_{PTC}, respectively). Gradient lengthscale exhibits similar ratiometric behavior (Fig. 2E).

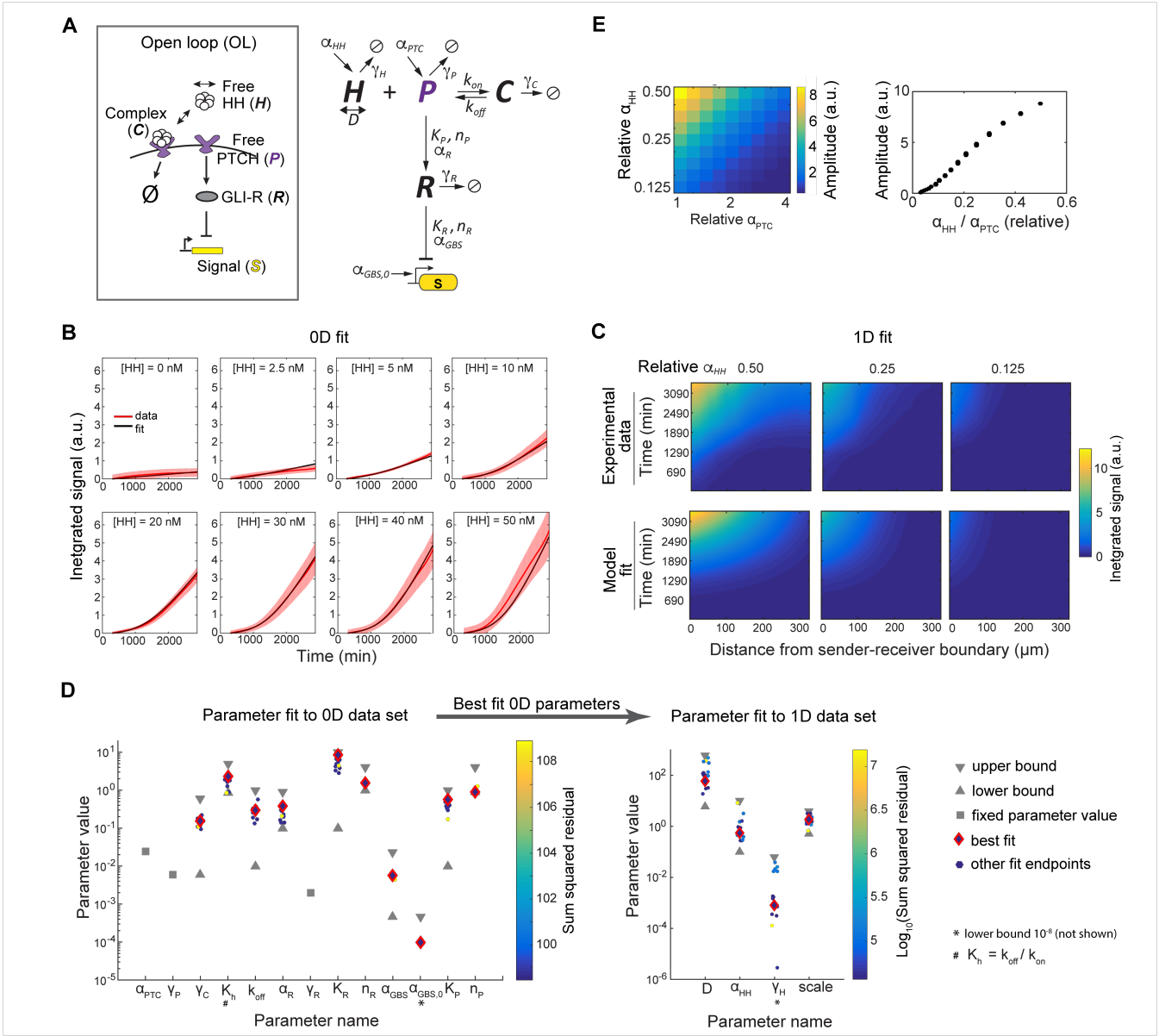

Fig. S5. A simple, GLIR-only model captures experimentally-observed open loop dynamics.

(A) Open loop model (Eqs. C.1-8 in supplementary text). *H,* HH; *P*, free PTCH; *S*, signal; *C*, HH-PTCH complex; *R*, GLIR transcription factor. Free PTCH inhibits pathway activity by upregulating production of the repressor GLIR, which in turn inhibits signaling. When free PTCH is depleted by HH binding, new GLIR production ceases, and the existing pool of GLIR must decay below concentration K_R in order to initiate signaling; the slow decay of GLIR levels after HH exposure explains the observed time delay between ligand exposure and the initiation of signaling (Fig. S1C). Arrows between *H*, *P*, and *C* indicate synthesis, degradation, binding and unbinding. The arrow from *P* to *R* indicates Hill-type activation of *R* synthesis with the indicated parameters [half-maximal activation level of PTCH (K_p), Hill coefficient (n_p), and maximum production rate (α_r)]. Finally, the inhibitory arrow from *R* to *S* indicates a repressing Hill-type regulatory effect with indicated parameters [half-maximal inhibitory level of GLIR (K_R), Hill coefficient (n_R), and maximum GLIR-regulated promoter activity (α_{GBS})]. **(B-D)** Parameter values were determined by a two-step, least-squares fitting procedure. (B) First, a non-spatial, cell-autonomous version of the model (materials and methods, and Eqs. C.1-5) was globally fit to an SHH titration experiment in which rmSHHN was supplied at fixed concentrations via bath application (results from Fig. S3D). Fitting sought to minimize the weighted sum of squared residuals, which was calculated by summing the square of the difference between each datapoint and the corresponding model prediction, weighted by the standard deviation of the data at each point. (C) Next, the additional parameters needed for the spatial model — the diffusion constant *D*,

ligand production rate α_{HH}, ligand first-order degradation rate γ_H, and a scaling factor relating the signaling intensity observed in the spatial datasets to those in the bath titration datasets — were determined by globally fitting the model to three spatiotemporal datasets (sender densities of 12.5%, 25%, and 50%) using open loop receivers with relative a_{PTC} = 1.0. In this fit, the cell-autonomous parameters obtained from the bath titration fit (fig S5B) were fixed. As with the cell-autonomous fits, the residual between the data and model was weighted by the standard deviation of the data (see materials and methods). The cell-autonomous and spatial fits were run 10-15 times each, with the fits initialized with parameter guesses logarithmically distributed between reasonable bounds estimated from literature; the parameters resulting from the best fit (smallest weighted least squares) were chosen (see also Table S2). The upper and lower parameter bounds (*gray triangles*), parameter values obtained from each run (*solid dots*), and the parameters obtained from the best overall fit (*red diamond*) are shown in (D). **(E)** The model predicts that the amplitude of the signaling gradient depends ratiometrically on the ligand and receptor production rates (α_{HH} and α_{PTC}, respectively), as observed experimentally (Fig. S4D).

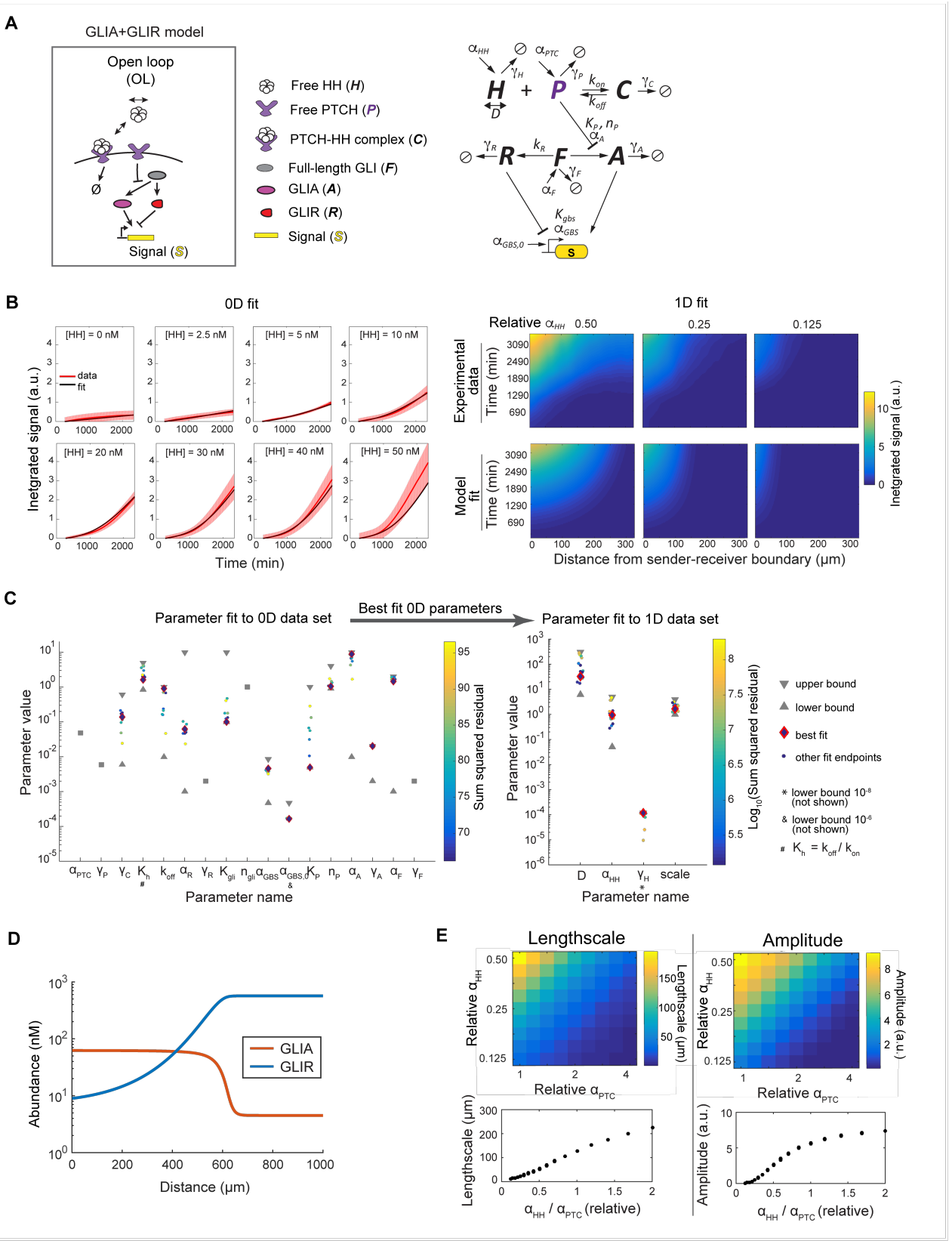

Fig. S6. Explicit modeling of both GLIA and GLIR also captures experimentally-observed open loop dynamics and produces ratiometric behavior.

(A) Open loop GLIA+GLIR model (Section E in supplementary text). *H,* HH; *P*, free PTCH; *S*, signal; *C*, HH-PTCH complex; *F*, full-length GLI; *R*, GLIR transcription factor; *A*, GLIA transcription factor. Free PTCH inhibits pathway activity by repressing the production of GLIA. Arrows between *H*, *P*, and *C* indicate synthesis, degradation, binding and unbinding rates. Arrow from *P* to *A* indicates Hill-type inhibition of *A* synthesis with the indicated parameters. Finally, the inhibitory arrow from *R* to *S* and the activating arrow from *A* to *S* indicate transcriptional regulation by both *A* and *R* with indicated parameters. For simplicity, we assume that there are two GLI binding sites controlling production of *S* (*18*, *48*). When both sites are bound by GLIA, the transcriptional output is twice that produced when one site is bound by GLIA and the other is unbound; when one or two GLIRs are bound, the promoter is fully repressed, except for a constitutive, leaky production rate of $a_{GBS,0}$. **(B-C)** Parameters in the model were determined using the same two-step, least-squares fitting procedure as in Fig. S5B-D. **(D)** The steady-state spatial distribution of GLIA and GLIR at relative α_{HH} = 1.0 shows that GLIA predominates proximal to the source, while GLIR predominates at distal regions. **(E)** The amplitude and lengthscale of the signaling gradient depend ratiometrically on the ligand and receptor production rates (α_{HH} and α_{PTC}, respectively).

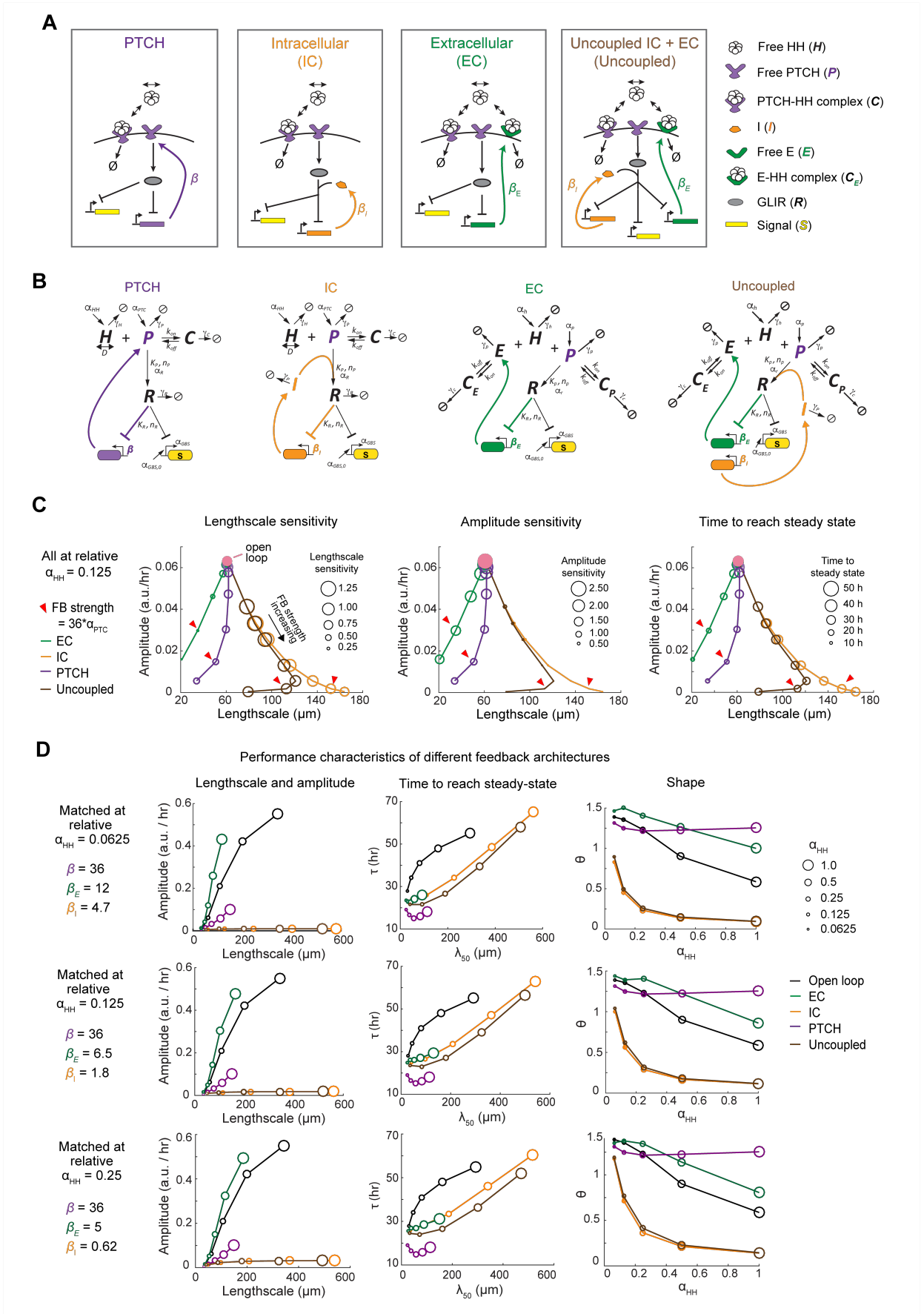

Fig. S7. Comparison of different negative feedback architectures in the GLIR-only model

(A) Cartoons describing the PTCH, intracellular (IC), extracellular (EC), and uncoupled negative feedback models. The only free parameters – those not determined by the open loop fit (Fig. S5) – are the feedback strengths β, β_I and β_E, describing the strengths of PTCH, IC, and EC feedbacks, respectively. These feedbacks are experimentally tunable by changing the concentration of Dox. **(B)** Detailed schematic of the feedback models (Eqs. D.1-26). The PTCH feedback model adds negative feedback to the open loop model in Fig. S5A. *P* now has two production terms: a constitutive term α_{PTC} and an additional term negatively controlled by *R* (purple arrows). The feedback acts negatively overall, since signaling leads to upregulation of *P*, which in turn inhibits signaling in two ways (due to the bifunctionality of PTCH): first, by upregulating *R* production and, second, by reducing the extracellular ligand concentration *H* through sequestration and degradation. The strength of the feedback is set in the model by a parameter β, which is the ratio between the maximum rate of feedback-regulated *P* production and the rate of *P* produced constitutively. In Fig. 3, β is set to 36 to match the experimentally-observed fold upregulation of *P* production (as reported by mCherry levels) in receivers immediately adjacent to a sender field consisting of 100% senders. IC and EC feedbacks are implemented by proteins *I* and *E*, respectively. The biochemical parameters for *I* and *E* are identical to those of PTCH except that *I* cannot bind ligand and *E* does not regulate GLIR production. Uncoupled feedback includes both *I* and *E*, incorporated in the same manner as for IC and EC feedbacks. **(C)** Feedback models differ systematically, regardless of feedback strength. Each plot shows the lengthscale and amplitude of the gradient for each of the four feedback models at different feedback strengths (positions along curves), all at relative α_{HH} = 0.125. The plots differ in the meaning of the marker size, which indicates lengthscale sensitivity (*left*), amplitude sensitivity (*middle*), or time to reach steady-state (*right*). Red arrowheads mark a feedback strength of β = 36. Feedback strength differs four-fold between adjacent markers. EC feedback (*green*) enhances lengthscale robustness (i.e., lowers lengthscale sensitivity) at the cost of decreasing lengthscale and amplitude. IC feedback (*orange*) enhances amplitude robustness (i.e., lowers amplitude sensitivity) at the cost of decreasing amplitude and increasing lengthscale. When the IC and EC feedbacks are combined with the same feedback strengths in the uncoupled model (*brown*), the system behaves similarly to the IC feedback model across the entire range of feedback strength. In contrast, PTCH feedback (*purple*) increases both lengthscale robustness and amplitude robustness, with feedback strength affecting primarily amplitude (lengthscale is less sensitive to feedback strength). PTCH feedback also provides, along with EC feedback, the greatest acceleration of gradient formation. **(D)** The qualitative differences amongst the feedback architectures persist across sender strengths. By tuning β_I and β_E, the amplitude of the IC model and the lengthscale of the EC model can be matched, at any particular value of α_{HH}, to that of the PTCH model. The uncoupled model adopts those fine-tuned values of β_I and β_E. Given this tuning, the properties of the models diverge as α_{HH} is changed. The PTCH feedback strength is fixed at 36 in all panels. The plots in the top row are identical to those in Fig. 3B, C and E.

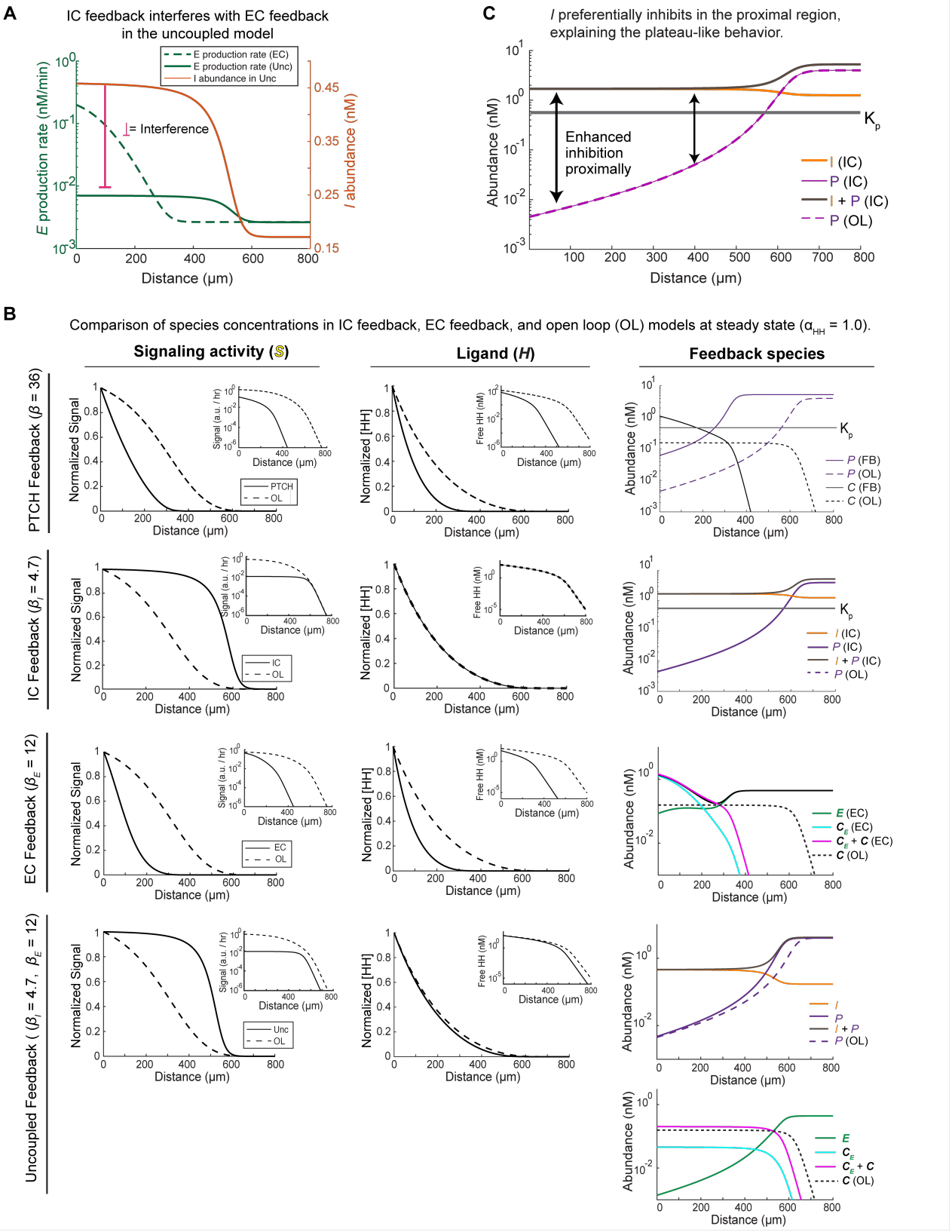

Fig. S8. Steady-state distributions of ligand, feedback species, and signaling levels explain the origin of interference in the uncoupled model and the increase of lengthscale in the IC model.

(A) Interference between IC and EC feedbacks in the uncoupled model. HH induces upregulation of both *I* and *E*. *E* levels become depleted due to binding to *H*, but *I* (*orange solid line*), which is not antagonized by *H*, simply accumulates. Accumulating levels of *I* dampen (*magenta inhibitory arrow*) production of *E* (*green solid line*),

preventing replenishment of *E* levels. In contrast, in the EC model, *E* production (*dotted green line*) is much stronger near the source, allowing replenishment of depleted *E*. All feedback strengths are identical to the ones used in Fig. 3. The marked difference between the *E* production rates in the uncoupled and EC models (*solid* and *dotted green lines*, respectively) — despite identical values of β_E — is due to the presence of *I* in the uncoupled model. **(B)** Steady-state spatial distributions of signaling activity (*left*), ligand levels (*center*), and feedback species (*right*) for different feedback models. All plots use relative α_{HH} = 1.0 and the same feedback strength (β, β_I or β_E) used in Fig. 3. In the open loop (OL), PTCH feedback, and EC feedback models, perception roughly follows ligand concentration. By contrast, in the IC and uncoupled models, the perception profile shows a plateau relative to the ligand, suggesting plateau-like shapes in perception gradients could be indicative of intracellular negative feedback. **(C)** IC feedback preferentially inhibits signaling activity in the proximal region. In the open loop (OL) model, signaling activity is inversely dependent on the abundance of free PTCH (*P, dashed magenta line*); in the IC model, signaling activity is inversely dependent on the sum of *P* and *I* (*P*, *solid magenta line; I, solid orange line*; and *I* + *P*, *solid cyan line*). The level of inhibitory species at which signaling is half-maximally downregulated is K_P. The ratio between the inhibitory species in the two models — *I* + *P* (*cyan*) in the IC mode versus *P* (*dotted magenta line*) in the OL model — is much greater proximal to the senders. The greater level of inhibition in the proximal vs distal region (*black arrows*) means that signaling is disproportionally inhibited in the proximal region. This flattens the shape of the signaling gradient (plot of normalized signal perception in (B)) proximally. This plateauing, in turn, leads to increased lengthscale, as lengthscale is defined as the distance at which the signaling activity decreases to 1/e of its value in the most proximal cell. At the same time, a “threshold lengthscale”, defined as the distance at which a certain absolute level of signaling is reached, decreases due to the reduction in signaling activity everywhere.

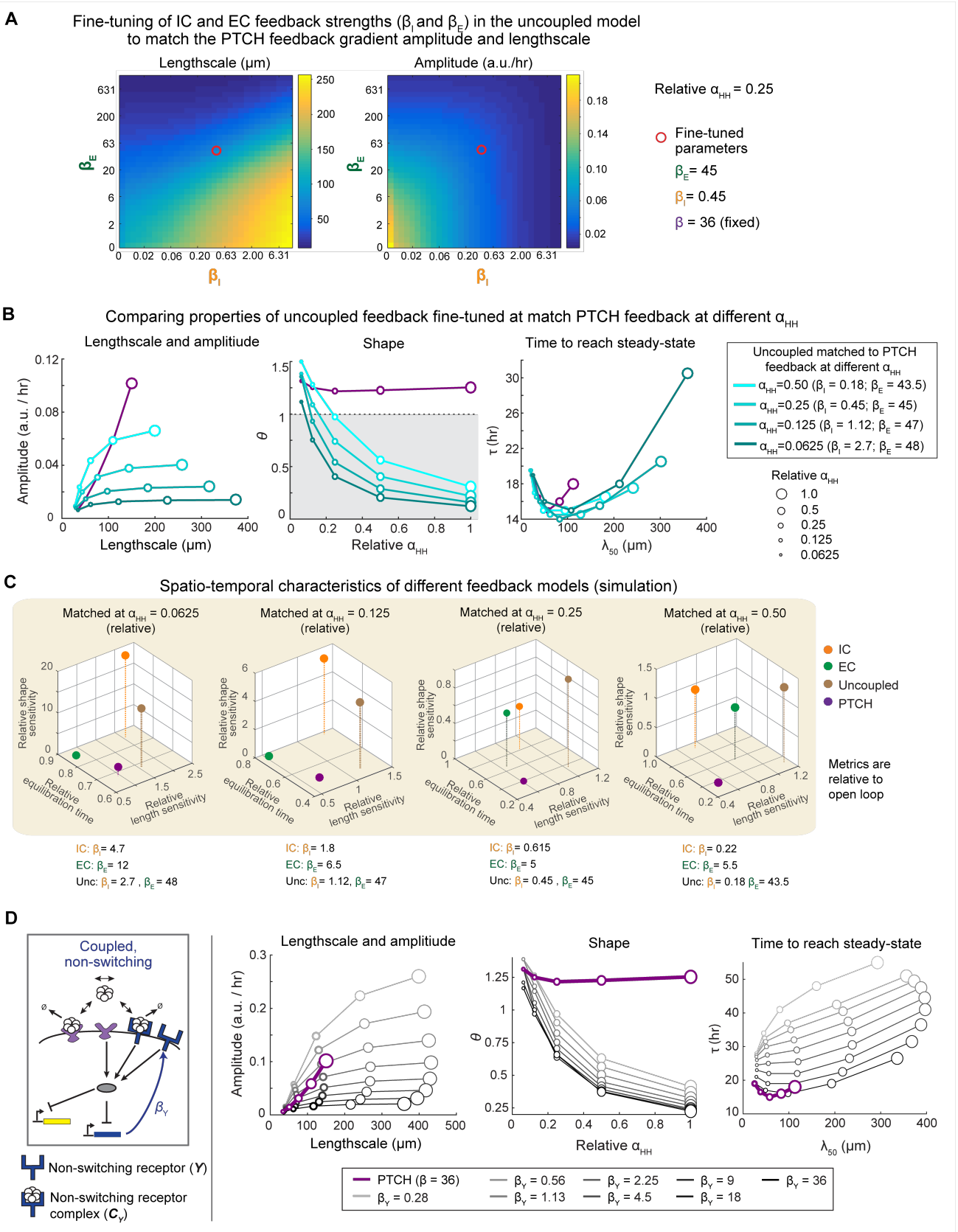

Fig. S9. The uncoupled model underperforms PTCH feedback even when the component feedback strengths are fine-tuned.

(A) Dependence of steady-state lengthscale and amplitude on the two feedback strengths (β_I and β_E) in the uncoupled feedback model at relative α_{HH} = 0.25. *Red circles* denote values of β_I and β_E fine-tuned to produce a lengthscale and amplitude equal to that of PTCH feedback at β = 36. **(B)** Comparison of steady-state signaling gradients produced by PTCH and uncoupled feedbacks, with the uncoupled feedback strengths (β_I and β_E) individually fine-tuned, as shown in (A), to match the lengthscale and amplitude of PTCH feedback at different values of α_{HH} (different shades of cyan). PTCH feedback strength β was set at 36. Regardless of the fine-tuned values of β_I and β_E, the uncoupled model systematically diverges from the PTCH model. However, in some cases, fine-tuning allows the uncoupled model to reach steady state slightly faster than the PTCH feedback model. **(C)** The evolutionarily-conserved PTCH feedback outperforms alternative pathway architectures in enhancing the lengthscale robustness, shape robustness, and speed of formation of signaling gradient. Performance differences are systematically preserved across different feedback strengths and ligand production rates. Performance is measured relative to that of the open loop model, which has a value of 1 in each dimension. The PTCH feedback strength was fixed at 36 across different α_{HH} values. The feedback strengths for other models were independently tuned at a given α_{HH} so that the amplitude of the IC model, lengthscale of the EC model, and both the amplitude and lengthscale of the uncoupled model match the corresponding properties of the PTCH feedback model. The plot representing the matching point at α_{HH} = 0.25 is identical to Fig. 4F. **(D)** Performance of the coupled, non-switching model. In this model, a hypothetical receptor-like molecule *Y* physically couples intracellular and extracellular activities. Y acts like PTCH to bind HH, but both the ligand-free and ligand-bound states suppress the intracellular signal (cartoon on the *left*; compare to the cartoons in Fig S7A). The only free parameter is the feedback strengths β_Y. (*Right*) Comparison of steady-state signaling gradients produced by PTCH feedback and coupled, non-switching feedback. The PTCH feedback strength β was set at 36. The coupled, non-switching model is shown for a variety of feedback strengths β_Y. Note that regardless of the value of β_Y, the coupled, non-switching model underperforms the PTCH model in terms of amplitude robustness, lengthscale robustness, shape robustness, and time to reach steady state.

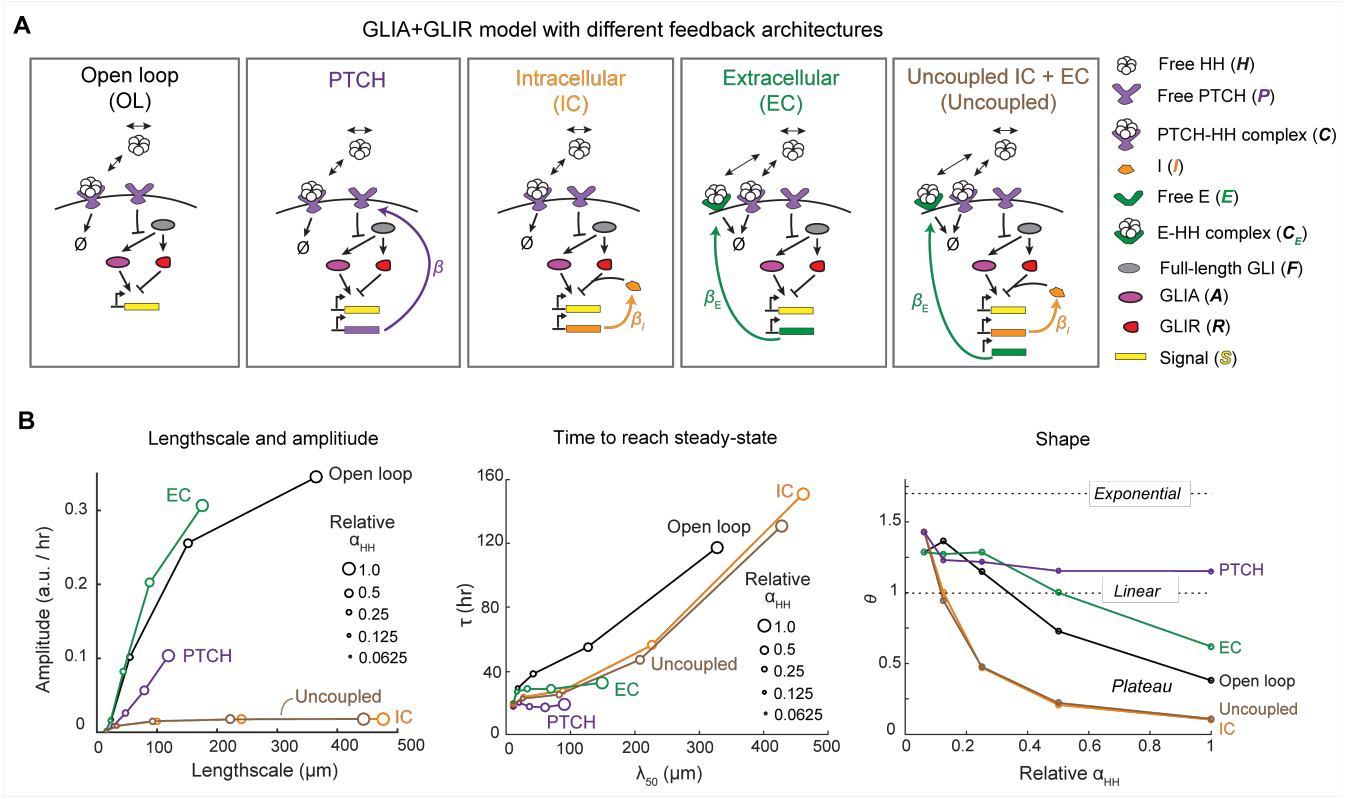

Fig. S10. PTCH Feedback outperforms other feedback designs in the GLIA+GLIR model.

(A) Cartoons describing the open loop, PTCH, intracellular (IC), extracellular (EC), and uncoupled negative feedback models that incorporate full-length GLI (*F*), GLIA (*A*) and GLIR (*R*). The only free parameters – those not determined by the open loop fit (Fig. S6) – are the feedback strengths β, β_I and β_E, describing the strengths of PTCH, IC, and EC feedbacks, respectively. (Section E in supplementary text). These feedbacks are tunable experimentally by changing the concentration of Dox. **(B)** Steady-state gradient properties for different models. *Left*: length and amplitude as a function of α_{HH} (marker size); *middle*: time to reach steady state (τ) for each model as a function of λ_{50} and α_{HH}; *right*, gradient shape (θ) as a function of α_{HH}. The definitions of λ_{50}, τ and θ are the same as in Fig. 3. The qualitative differences between different feedback models are preserved in the GLIA+GLIR model. PTCH feedback strength β was set to 16 to match the experimentally-observed fold upregulation of *P* production (as reported via mCherry levels) in receivers immediately adjacent to a field of 100% senders. The feedback strengths of the IC and EC models were fine-tuned (β_I=1.04 and β_E=16) so that the amplitude or lengthscale, respectively, matches that of PTCH feedback at α_{HH} = 0.0625. Those same feedback strengths were used for the uncoupled model.

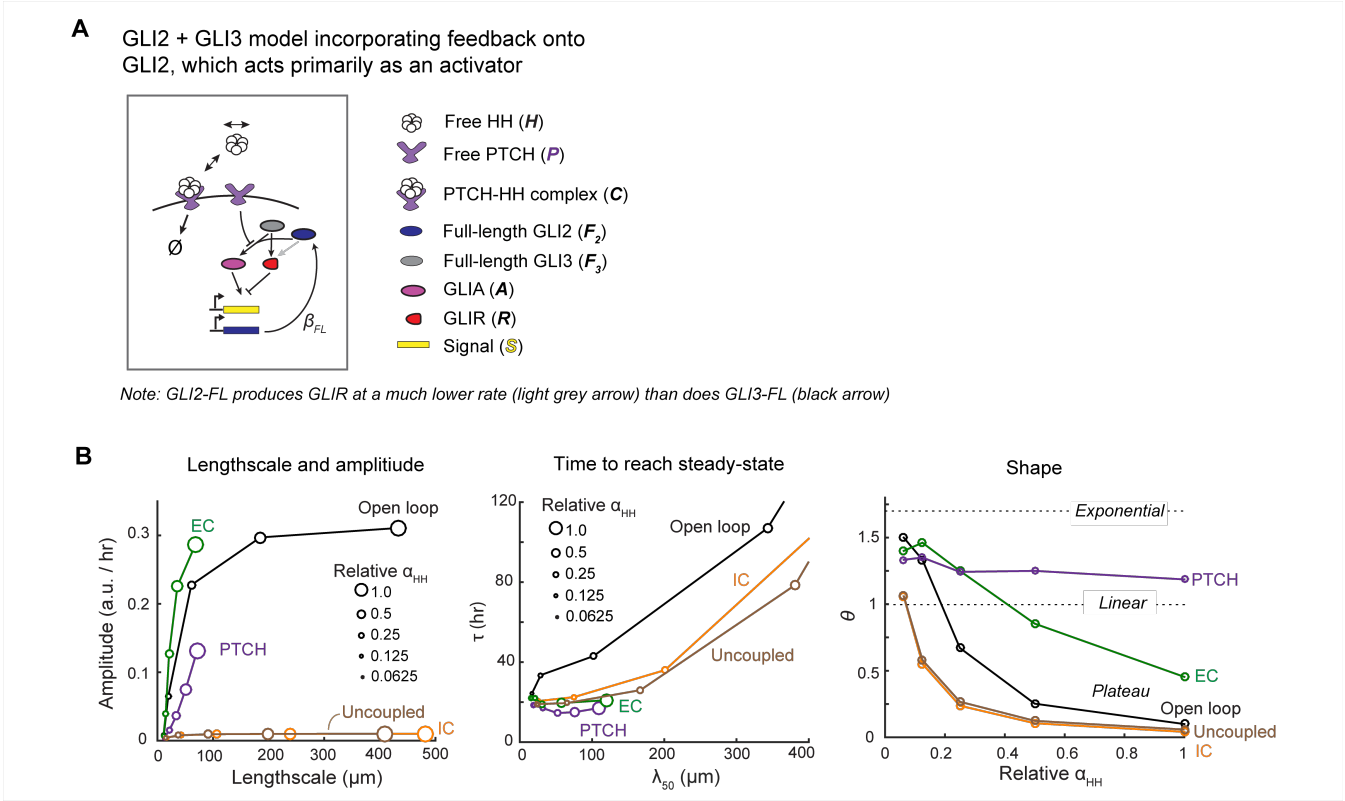

Fig. S11. PTCH feedback outperforms other feedback designs in the GLI2+GLI3 model.
(A) Cartoon of a model incorporating both GLI2 and GLI3 to explicitly simulate a moderate upregulation of GLI2 expression upon signal activation. F_2, full-length GLI2; F_3, full-length GLI3; *R*, GLIR transcription factor; *A*, GLIA transcription factor. The rate of GLIR production from F_2 (*light gray arrow*) is much smaller than the rate from F_3 (*black arrow*), making GLI2 primarily a transcription activator. The model does not distinguish the *A* or *R* produced by F_2 versus F_3. Free PTCH inhibits the pathway activity by repressing the production of *A* from both F_2 and F_3. Arrows between *H*, *P*, and *C* indicate synthesis, degradation, binding and unbinding rates. The inhibitory arrow from *R* to *S* and the activating arrow from *A* to *S* indicate transcriptional regulation by both *A* and R, with the same functional form as in the GLIA+GLIR model. Finally, the signal controls the production of F_2 — a positive feedback — at the strength of β_{FL} (Section F in supplementary text). Parameters in the model were determined using the same two-step, least-squares fitting procedure as in Fig. S5B-D (Table S2). The fit value for β_{FL} tends to produce less GLI2 compared to the experimentally measured 2-fold increase in the *Gli2* mRNA level. To ensure that we are assessing the effects of non-trivial levels of GLI2 upregulation, we turned up β_{FL} to 2.4 for subsequent analysis. **(B)** Steady-state gradient properties for different models. *Left*: lengthscale and amplitude as a function of α_{HH} (marker size); *middle*: time to reach steady state (τ) for each model as a function of λ_{50} and relative α_{HH}; *right*, gradient shape (θ) as a function of relative α_{HH}. The definitions of λ_{50}, τ and θ are the same as in Fig. 3. The qualitative differences between different feedback models are preserved in the GLI2+GLI3 model. The PTCH feedback strength β was set to 16 to match the experimentally-observed fold upregulation of *P* production (as reported via mCherry levels) in receivers immediately adjacent to a sender field consisting of 100% senders. The feedback strengths for the IC and EC models were fine tuned (β_I = 2.4 and β_E = 8) so that the amplitude or lengthscale, respectively, matches that of PTCH feedback at α_{HH} = 0.0625. Those same feedback strengths were used for the uncoupled model. Note that the addition of GLI2 feedback systematically slows the time to approach steady states, consistent with previous reports on the role of positive feedback (*49*, *50*). This does not change the qualitative conclusions about the relative behaviors of different types of feedback.

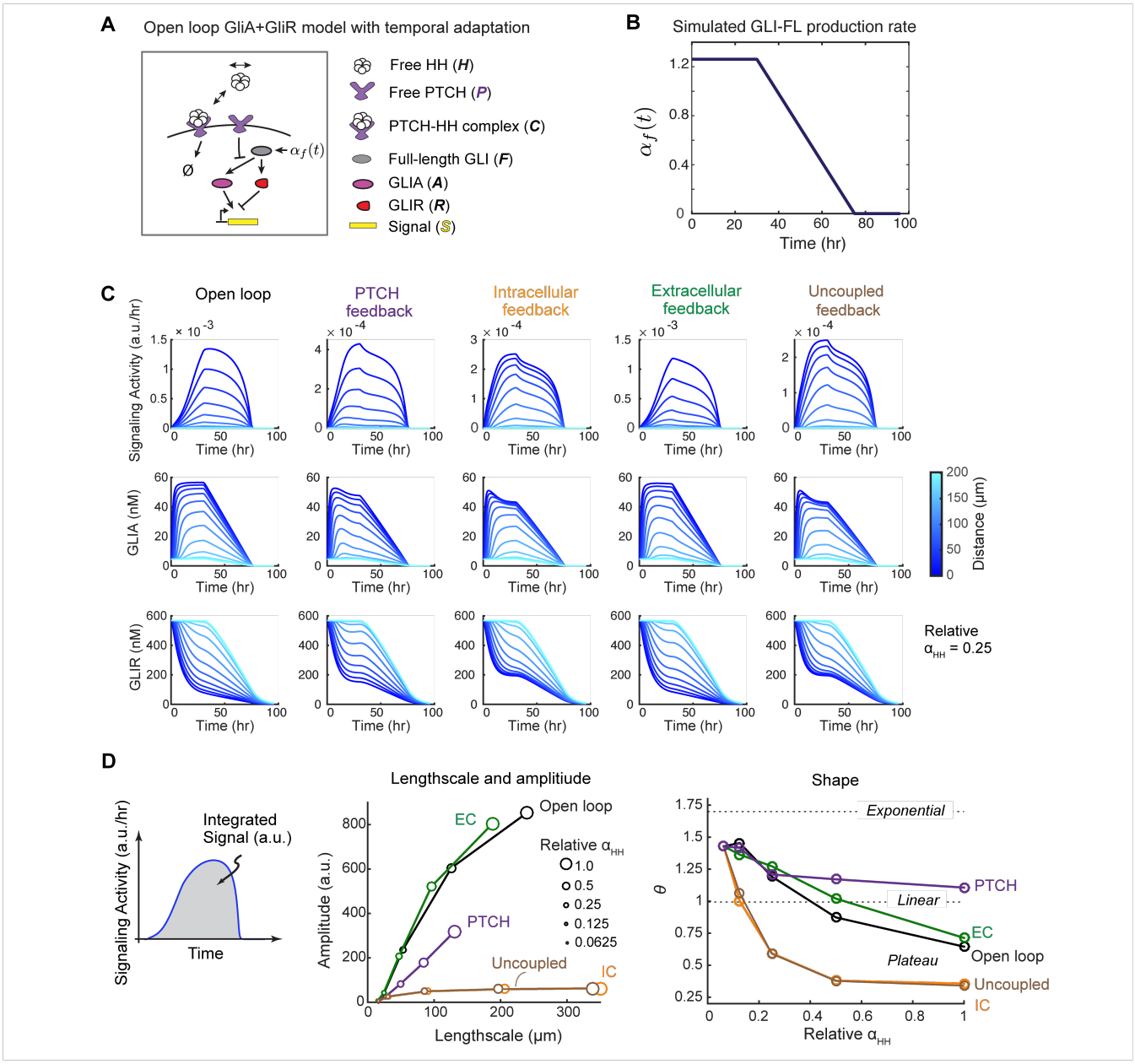

Fig. S12. PTCH feedback outperforms other feedback designs in the presence of temporal adaptation.
(A) Temporal adaptation, which is weak or non-existent in our other models, was simulated by making the production rate of full-length GLI time-dependent ($\alpha_f(t)$), with production decreasing over time. Otherwise, the model is identical to the GLIA+GLIR model described in Fig. S6. Feedback models incorporate the same time-dependent production of full-length GLI. *In vivo*, temporal adaptation is a feature in some, but not all, SHH morphogenetic contexts. This variation in occurrence suggests that adaptation is not an intrinsic feature of the pathway but rather could result from mechanisms such as downregulation of SHH synthesis or downregulation of full-length GLI expression (*18*), with the latter explicitly modeled here. **(B)** $\alpha_f(t)$ is a piecewise linear function that declines to zero between 30-75 hrs, to match the timing of adaptation previously reported in the mouse neural tube *(10).* **(C)** Temporal profiles of signaling activity (*top row*), GLIA abundance (*middle row*), and GLIR abundance (*bottom row*) in different models with temporal adaptation. Shades of blue represent the distance away from the source. Feedback strengths are identical to those in Fig. S10. **(D)** Performance of the different feedback models in the presence of adaptation. *Left:* because steady-state signaling activity is 0 in all models, we instead analyzed the temporally integrated signal (area under curve); *middle*: length and amplitude as a function of α_{HH} (marker size); *right*, gradient shape (θ) as a function of α_{HH}.

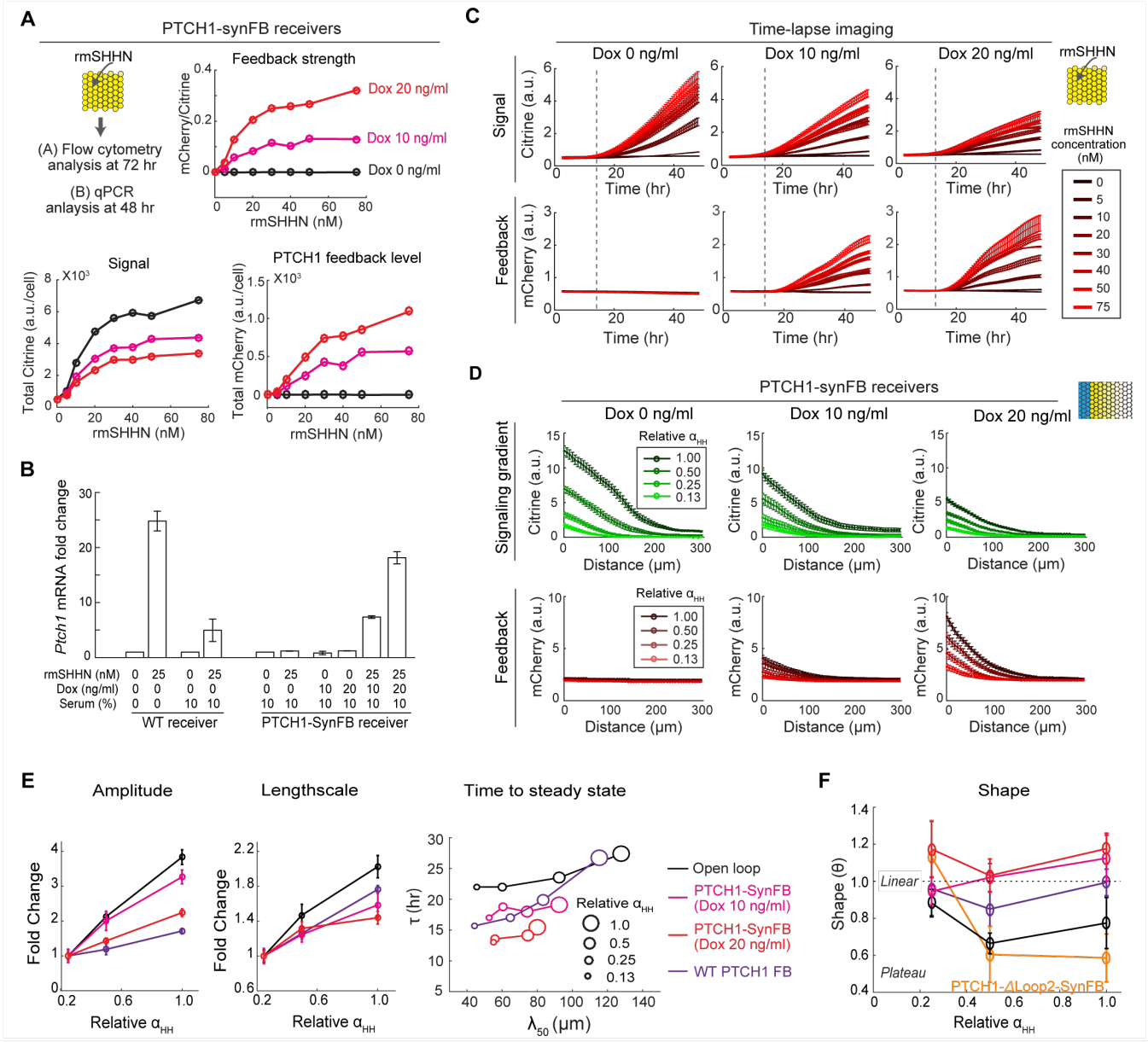

Fig. S13. Characterization of the PTCH1-SynFB receiver cell line (as shown in Fig. 4A).

(A) Synthetic PTCH1 feedback reduces the overall signaling response to rmSHHN (*bottom left*). The amount of PTCH1, indicated by mCherry level (*bottom right*), depends on both SHH and Dox concentrations. No increase in mCherry was observed in the absence of Dox (black line) or SHH (0 nM rmSHHN data points). The Dox concentration controls the strength of the feedback, as indicated by the ratio between mCherry and Citrine (*top*). All data represent mean of population distributions obtained by flow cytometry after 72 hr of indicated treatment. **(B)** The feedback strength of PTCH1-SynFB can be tuned to be similar to, or even stronger than, the strength of PTCH feedback in wild-type (WT) NIH3T3 cells, quantified by qRT-PCR after 48 hrs of treatment. Notice that at the same rmSHHN concentration, WT cells had higher fold change in *Ptch1* expression without serum than with 10% serum. However, to keep cells relatively healthy, all the gradient experiments were performed with 10% serum in the media. **(C)** Time-lapse imaging shows that mCherry dynamics follow the Citrine reporter dynamics under constant rmSHHN and Dox concentrations. rmSHHN and Dox were added to SynFB receivers at 0 hr, and dynamics were recorded by time-lapse imaging. Each time trace represents the population average under the given combination of rmSHHN and Dox concentrations. *Dashed lines* indicate the time when Citrine signal activity (*top plots*) becomes detectable. These results show that the feedback is not "leaky" and is activated shortly after signaling begins. Each trace averages over 10 fields of view. **(D)** PTCH1-

SynFB reduces gradient sensitivity to variations in α_{HH} experimentally. The effects depend on the strength of the feedback, controlled by Dox concentration. *Top row*, total Citrine representing temporally integrated signaling gradient (same data as Fig. 4D, without normalization); *bottom row*, total mCherry representing the amount of feedback. Gradients were reconstituted using the senders described in Fig. 1C induced with 100 nM 4-OHT, and imaged at 42.5 hr. **(E)** PTCH1 feedback improved amplitude (*left panel*) and lengthscale (*middle panel*) robustness to variations in ligand production rates, as well as accelerated the approach to steady state (*right panel*). The performance depends on the strength of PTCH1 feedback, and WT cells behaved similarly to PTCH1-SynFB cells at intermediate feedback strength. Data shown as mean ± s.e.m. (n=10 each). **(F)** Quantification of gradient shape for different pathway architectures and feedback strengths. Both WT NIH3T3 cells (*purple*) and PTCH1-SynFB (*magenta* and *red*) improved the linearity of the gradient. Both open loop (*black*) and PTCH1-ΔLoop2-SynFB (IC feedback at 75 ng/ml Dox, *orange*) displayed plateau-like gradient shapes at high α_{HH}. Data shown as mean ± s.e.m. (n=10 each).

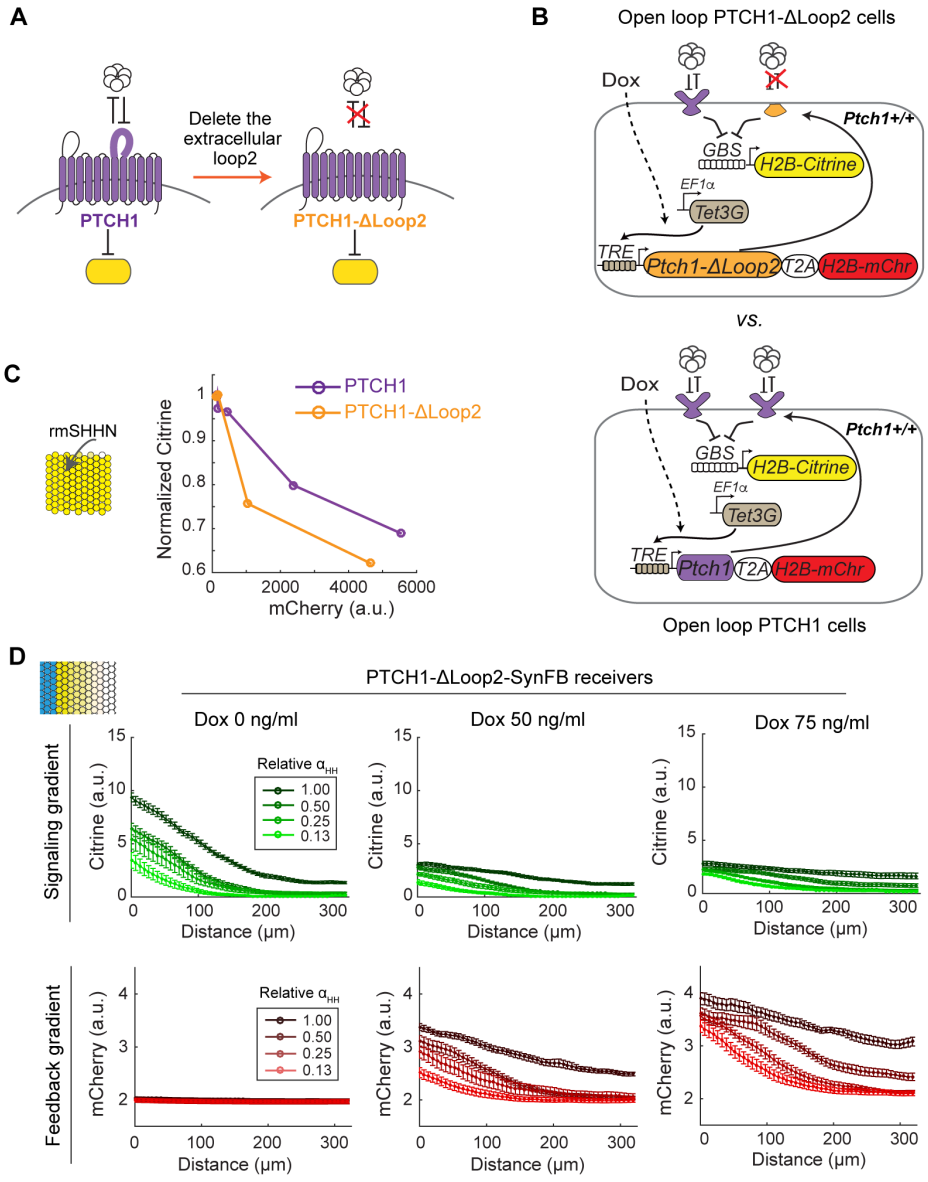

Fig. S14. Characterization of open and closed loop PTCH1-ΔLoop2 receiver cells.
(A) Design of the PTCH1-ΔLoop2 mutant. An extracellular loop was deleted to eliminate its interaction with HH (*25*). **(B)** PTCH1-ΔLoop2 or PTCH1 were integrated into wild-type receiver cells in the open loop configuration, with the expression level tuned by Dox concentrations, reported by the mCherry (mChr) level. **(C)** The open loop receiver cells show decreased signaling activity (Citrine) with increasing level of PTCH1 or PTCH1-ΔLoop (mCherry). Notice that at a given mCherry level, PTCH1-ΔLoop2 is more effective at suppressing intracellular signaling than PTCH1. This is because ligand binding inactivates PTCH1, but PTCH1-ΔLoop2 is unaffected by SHH. At the same protein production rate, a higher level of free PTCH1-ΔLoop2 protein will accumulate, leading to stronger suppression of intracellular signaling activity. Cells were treated with 50 nM rmSHHN at 0 hr and analyzed by flow cytometry at 48 hrs. **(D)** IC feedback enhances the robustness of gradient amplitude to variations in ligand production rates. Reconstituted linear gradients with PTCH1-ΔLoop2 closed loop receivers (same experiment as Fig. 4E). Feedback strength can be tuned with Dox from no feedback (0 ng/ml) to high feedback (75 ng/ml). *Top row*, total Citrine representing temporally integrated signaling gradient; *bottom row*, total mCherry representing the amount of feedback. Gradients were reconstituted using the senders constructed in Fig. 1C induced with 100 nM 4-OHT, and imaged at 42.5 hr.

Tables

Table S1. The expression level of HH pathway components

Category	Gene	Locus	Untreated (FPKM)	rmSHHN treated (FPKM)	Fold change (rmSHHN/Untreated)
Ligands	*SHH*	chr5:28456839-28719209	0	0	N/A
	Dhh	chr15:98893026-98898540	0	0	N/A
	Ihh	chr1:74945317-74951651	0.11	0	N/A
Gli Transcription Factors & Signal Transduction Components	*Gli1*	chr10:127323726-127341579	1.21	27.32	22.58
	Gli2	chr1:118834060-119053619	6.33	11.23	1.77
	Gli3	chr13:15463722-15730025	7.36	6.57	0.89
	Ptch2	chr4:117096355-117114831	0	0.21	N/A
	Ptch1	chr13:63511532-63565520	4.00	38.63	9.66
	Smo	chr6:29735496-29761366	75.68	69.99	0.92
	Sufu	chr19:46396917-46486660	16.13	16.36	1.01
	Kif7	chr7:79660195-79714186	4.33	4.65	1.07
	Cul3	chr1:80266817-80340430	63.99	58.24	0.91
	Spop	chr11:95414082-95493410	71.98	74.07	1.03
Co-receptors & other HH-binding proteins	*Boc*	chr16:44485044-44558870	1.54	1.65	1.07
	Cdon	chr9:35452075-35507652	22.81	32.15	1.41
	Gas1	chr13:60174404-60177535	475.98	385.43	0.81
	Lrp2	chr2:69424334-69586067	0.02	0	N/A
	Hhip	chr8:79965850-80058008	0	0	N/A
	Hhat	chr1:192512827-192771219	12.25	14.71	1.20
	Disp1	chr1:183086263-183221529	7.89	7.48	0.95
	Disp2	chr2:118779718-118795175	0.29	0.57	1.97
	Scube2	chr7:109798690-109865679	0.13	0.05	0.38
	Notum	chr11:120653788-120660837	0	0	N/A

Table S2. Parameters used in the computational models

GLIR-only Model (Fig. 2-4, figs. S5 and 7-9, Eqs. C.1-6 and D.1-26)			
Parameter	**Description**	**Units**	**Fitted value**
α_{PTC}	Free PTCH Production rate	nM min^{-1}	0.024‡
γ_P	Free PTCH degradation rate constant	min^{-1}	0.006‡
γ_C	HH-PTCH degradation rate constant	min^{-1}	0.1539
K_h	HH-PTCH dissociation constant	nM	2.2771
k_{off}	HH-PTCH complex dissociation rate constant	min^{-1}	0.3018
K_P	Hill constant for PTCH control of GLIR production	nM	0.5660
n_P	Hill coefficient for PTCH control of GLIR production	unitless	0.9
α_R	GLIR production rate constant	nM min^{-1}	0.3908
γ_R	GLIR degradation rate constant	min^{-1}	0.002‡
K_R	Hill constant for GLIR control of signal production	nM	8.5184
n_R	Hill coefficient for GLIR control of signal production	unitless	1.5735
α_{GBS}	GLIR-dependent signal production rate constant	a.u. min^{-1}	$5.6881*10^{-3}$
$\alpha_{GBS,0}$	Basal (GLIR-independent) signal production rate constant	a.u. min^{-1}	$9.8715*10^{-5}$
D	Free HH diffusion constant	μm^2 min^{-1}	58.3931
α_{HH}	HH flux into receiver field at 100% sender strength	nM min^{-1}	0.5431
γ_H	Free HH degradation rate constant	min^{-1}	$8.1346*10^{-4}$
β	PTCH feedback strength, as fold increase over α_{PTC}	unitless	36
m	Multiplicative factor relating the amplitude in 1D experiments to that in 0D experiments (1D divided by 0D)	unitless	1.8657
GLIA+GLIR Model (figs. S6, 10 and 12, supplementary text Section E and G)			
Parameter	**Description**	**Units**	**Fitted value**
α_{PTC}	Free PTCH Production rate	nM min^{-1}	0.024‡
γ_P	Free PTCH degradation rate constant	min^{-1}	0.006‡
γ_C	HH-PTCH degradation rate constant	min^{-1}	0.1488
K_h	HH-PTCH dissociation constant	nM	2.5422

k_{off}	HH-PTCH complex dissociation rate constant	min^{-1}	0.6983
K_P	Hill constant for PTCH control of GLIR production	nM	0.0050
n_P	Hill coefficient for PTCH control of GLIR production	unitless	1.0986
α_R	Rate constant for GLIR production from full-length GLI	nM min^{-1}	0.0663
γ_R	GLIR degradation rate constant	min^{-1}	0.002‡
α_A	Rate constant for GLIA production from full-length GLI	nM min^{-1}	8.1436
γ_A	GLIA degradation rate constant	min^{-1}	0.02
α_F	Full-length GLI production rate constant	nM min^{-1}	1.2609
γ_F	Full-length GLI degradation rate constant	min^{-1}	0.002‡
K_{gli}	Hill constant for GLIA/R control of signal production	nM	0.1001
α_{GBS}	GLIR-dependent signal production rate constant	a.u. min^{-1}	0.0045
$\alpha_{GBS,0}$	Basal (GLIR-independent) signal production rate constant	a.u. min^{-1}	$1.6405*10^{-4}$
D	Free HH diffusion constant	μm^2 min^{-1}	32.3941
α_{HH}	HH flux into receiver field at 100% sender strength	nM min^{-1}	0.4740
γ_H	Free HH degradation rate constant	min^{-1}	$1.1593*10^{-4}$
β□	PTCH feedback strength, as fold increase over α_{PTC}	unitless	16
m	Multiplicative factor relating the amplitude in 1D experiments to that in 0D experiments (1D divided by 0D)	unitless	1.7042
GLI2+GLI3 Model (Fig. S11, supplementary text Section F)			
Parameter	**Description**	**Units**	**Fitted value**
α_{PTC}	Free PTCH Production rate	nM min^{-1}	0.024‡
γ_P	Free PTCH degradation rate constant	min^{-1}	0.006‡
γ_C	HH-PTCH degradation rate constant	min^{-1}	0.1067
K_h	HH-PTCH dissociation constant	nM	1.8124
k_{off}	HH-PTCH complex dissociation rate constant	min^{-1}	0.9157
K_P	Hill constant for PTCH control of GLIA production	nM	0.0100
n_P	Hill coefficient for PTCH control of GLIA production	unitless	1.3007
α_F	Full-length GLI2/3 production rate constant	nM min^{-1}	0.7610

γ_F	Full-length GLI2/3 degradation rate constant	min^{-1}	$0.002^{\ddagger}$
α_A	Rate constant for GLIA production from full-length GLI2/3	nM min^{-1}	1.9996
α_{R2}	Rate constant for GLIR production from full-length GLI2	nM min^{-1}	0.00326
α_{R3}	Rate constant for GLIR production from full-length GLI3	nM min^{-1}	0.0315
γ_A	GLIA degradation rate constant	min^{-1}	0.02^{0}
γ_R	GLIR degradation rate constant	min^{-1}	$0.002^{\ddagger}$
K_{gli}	Hill constant for GLIA and GLIR control of signal production	nM	0.1501
α_{GBS}	GLIA/R-dependent signal production rate constant	a.u. min^{-1}	0.0022
$\alpha_{GBS,0}$	Basal (GLI-independent) signal production rate constant	a.u. min^{-1}	$1.3854*10^{-4}$
D	Free HH diffusion constant	μm^2 min^{-1}	52.3942
α_{HH}	HH flux into receiver field at 100% sender strength	nM min^{-1}	0.4898
γ_H	Free HH degradation rate constant	min^{-1}	$7.644*10^{-6}$
β	PTCH feedback strength, as fold increase over α_{PTC}	unitless	16
m	Multiplicative factor relating the amplitude in 1D experiments to that in 0D experiments (1D divided by 0D)	unitless	2.5595
β_{FL}	GLI2 feedback strength, as fold increase over α_F	unitless	2.3797

‡ Fixed in the fit

Table S3. DNA constructs used in the study

Construct Name	Promoter	Gene	Refseq	Antibiotics	Role in this study
Super PiggyBac Transposase Expression Vector $	*CMV*	PiggyBac transposase	N/A	N/A	To facilitate the integration of target vectors
PB-PGK-ERT2-GAL4-T2A-H2B-mTurquoise2	*PGK*	*ERT2-GAL4*	N/A	Blastomycin	To generate inducible senders expressing mouse SHH
		H2B-mTurquoise2			
PB-UAS-SHH	*UAS*	*Shh*	NM_009170	Hygromycin	
PB-EF1a-Tet3G	*EF1α*	*Tet3G*§	N/A	Puromycin	To control the expression of mouse PTCH1
PB-GBS-miniCMV-H2B-Citrine	*8xGBS-miniCMV*	*H2B-Citrine*	N/A	Hygromycin	Reporter for HH pathway activity
PB-TRE3G-miniCMV-Myc-mPtch1-T2A-H2B-mCherry	*TRE3g-miniCMV* §	*Myc-Ptch1*	NM_008957	Blastomycin	To control the expression of mouse PTCH1
		H2B-mCherry	N/A		
PB-TRE3G-miniCMV-Myc-mPtch1-ΔLoop2-T2A-H2B-mCherry	*TRE3g-miniCMV* §	*Myc-mPtch1-ΔLoop2*	N/A	Blastomycin	To control the expression of mutant mouse PTCH1-ΔLoop2
		H2B-mCherry	N/A		
PB-GBS-miniCMV-Tet3G	*8xGBS-miniCMV*	*Tet3G* §	N/A	Puromycin	To control the expression Tet3G in the feedback circuit
pX330-U6-Chimeric_BB-CBh-hSpCas9(*51, 52*)	*Cbh*	*hSpCas9*	N/A	N/A	CRISPR backbone for knocking out *Ptch1*

$ Directly purchased from System Biosciences (#PB200PA-1)

§ Subcloned from the Tet-On® 3G Inducible Expression System (Clonetech, 631346)

Table S4. Nucleic Acid Oligo sequences used in the study

Name	Sequence	Role in the study
CRISPR03-gRNA02F	5'-CACCGCAGGGCGTGAGCGCTGTCA-3'	To generate CRISPR targeting *mPtch1*, forward strand
CRISPR03-gRNA02R	5'-AAACtgacagcgctcacgccctgc-3'	To generate CRISPR targeting *mPtch1*, reverse strand
*mPtch1*_F104	5'-CTCCTCATATTTGGGGCCTT-3'	qPCR primer for mouse *Ptch1*, forward
*mPtch1*_R104	5'-AATTCTCGACTCACTCGTCCA-3'	qPCR primer for mouse *Ptch1*, reverse
*mGli1*_F119	5'-GAGGTTGGGATGAAGAAGCA-3'	qPCR primer for mouse *Gli1*, forward
*mGli1*_R119	5'-CTTGTGGTGGAGTCATTGGA-3'	qPCR primer for mouse *Gli1*, reverse
*mTbp*_F109	5'-ACATCTCAGCAACCCACACA-3'	qPCR primer for mouse *Tbp*, forward
*mTbp*_R109	5'-GTGAAGGGTACAAGGGGGTG-3'	qPCR primer for mouse *Tbp*, reverse
*Citrine*_F96	5'-CACATGAAGCAGCACGACTT-3'	qPCR primer for *Citrine*, forward
*Citrine*_R96	5'-GGTCTTGTAGTTGCCGTCGT-3'	qPCR primer for *Citrine*, reverse

Movies

Movie 1: SHH signaling gradient formation in radial geometry with open loop receivers.

The movie shows representative SHH signaling gradient formation in radial geometry. Senders were induced with 100 nM 4-OHT at 0 hr, and no Dox was added. mTurquoise2 labels the sender cell nuclei, and Citrine reports the signal activity.

Movie 2: SHH signaling gradient formation in linear geometry with open loop receivers.

The movie shows representative SHH signaling gradient formation in linear geometry. Senders were induced with 100 nM 4-OHT at 0 hr, and no Dox was added. mTurquoise2 labels the sender cell nuclei, and Citrine reports the signal activity.

Movie 3-6: SHH signaling gradient formation in linear geometry with PTCH1-SynFB receivers.

The same senders and receivers were used for Movie 3-6. PTCH1 feedback is off in Movie 3-4 and on in Movie 5-6. Senders were induced with 100 nM 4-OHT at 0 hr for all movies, and receivers were induced with vehicle control or Dox at 0 hr. mTurquoise2 labels the sender cell nuclei, Citrine reports the signal activity, and mCherry reports the PTCH1 feedback level.

Movie 3: SHH signaling gradient formation with PTCH1-SynFB receivers at relative α_{HH} = 0.25 and 0 ng/ml Dox. (25% sender + 75% wild-type NIH3T3 cells in the sender region)

Movie 4: SHH signaling gradient formation with PTCH1-SynFB receivers at relative α_{HH} = 1.00 and 0 ng/ml Dox. (100% sender + 0% wild-type NIH3T3 cells in the sender region)

Movie 5: SHH signaling gradient formation with PTCH1-SynFB receivers at relative α_{HH} = 0.25 and 20 ng/ml Dox. (25% sender + 75% wild-type NIH3T3 cells in the sender region).

Movie 6: SHH signaling gradient formation with PTCH1-SynFB receivers at relative α_{HH} = 1.00 and 20 ng/ml Dox. (100% sender + 0% wild-type NIH3T3 cells in the sender region)

References and Notes

1. K. W. Rogers, A. F. Schier, Morphogen gradients: From generation to interpretation. *Annu. Rev. Cell Dev. Biol.* **27**, 377–407 (2011). doi:10.1146/annurev-cellbio-092910-154148 Medline

2. N. Perrimon, A. P. McMahon, Negative feedback mechanisms and their roles during pattern formation. *Cell* **97**, 13–16 (1999). doi:10.1016/S0092-8674(00)80710-2 Medline

3. M. Freeman, Feedback control of intercellular signalling in development. *Nature* **408**, 313–319 (2000). doi:10.1038/35042500 Medline

4. J. Briscoe, P. P. Thérond, The mechanisms of Hedgehog signalling and its roles in development and disease. *Nat. Rev. Mol. Cell Biol.* **14**, 416–429 (2013). doi:10.1038/nrm3598 Medline

5. Y. Chen, G. Struhl, Dual roles for patched in sequestering and transducing Hedgehog. *Cell* **87**, 553–563 (1996). doi:10.1016/S0092-8674(00)81374-4 Medline

6. L. Milenkovic, L. V. Goodrich, K. M. Higgins, M. P. Scott, Mouse patched1 controls body size determination and limb patterning. *Development* **126**, 4431–4440 (1999). Medline

7. J. Jeong, A. P. McMahon, Growth and pattern of the mammalian neural tube are governed by partially overlapping feedback activities of the hedgehog antagonists patched 1 and Hhip1. *Development* **132**, 143–154 (2005). doi:10.1242/dev.01566 Medline

8. L. V. Goodrich, R. L. Johnson, L. Milenkovic, J. A. McMahon, M. P. Scott, Conservation of the hedgehog/patched signaling pathway from flies to mice: Induction of a mouse patched gene by Hedgehog. *Genes Dev.* **10**, 301–312 (1996). doi:10.1101/gad.10.3.301 Medline

9. J. Taipale, J. K. Chen, M. K. Cooper, B. Wang, R. K. Mann, L. Milenkovic, M. P. Scott, P. A. Beachy, Effects of oncogenic mutations in Smoothened and Patched can be reversed by cyclopamine. *Nature* **406**, 1005–1009 (2000). doi:10.1038/35023008 Medline

10. N. Balaskas, A. Ribeiro, J. Panovska, E. Dessaud, N. Sasai, K. M. Page, J. Briscoe, V. Ribes, Gene regulatory logic for reading the Sonic Hedgehog signaling gradient in the vertebrate neural tube. *Cell* **148**, 273–284 (2012). doi:10.1016/j.cell.2011.10.047 Medline

11. D. Sprinzak, A. Lakhanpal, L. Lebon, L. A. Santat, M. E. Fontes, G. A. Anderson, J. Garcia-Ojalvo, M. B. Elowitz, Cis-interactions between Notch and Delta generate mutually exclusive signalling states. *Nature* **465**, 86–90 (2010). doi:10.1038/nature08959 Medline

12. A. D. Lander, Q. Nie, F. Y. M. Wan, Do morphogen gradients arise by diffusion? *Dev. Cell* **2**, 785–796 (2002). doi:10.1016/S1534-5807(02)00179-X Medline

13. M. Bischoff, A.-C. Gradilla, I. Seijo, G. Andrés, C. Rodríguez-Navas, L. González-Méndez, I. Guerrero, Cytonemes are required for the establishment of a normal Hedgehog morphogen gradient in *Drosophila* epithelia. *Nat. Cell Biol.* **15**, 1269–1281 (2013). doi:10.1038/ncb2856 Medline

14. X. Zeng, J. A. Goetz, L. M. Suber, W. J. Scott Jr., C. M. Schreiner, D. J. Robbins, A freely diffusible form of Sonic hedgehog mediates long-range signalling. *Nature* **411**, 716–720 (2001). doi:10.1038/35079648 Medline

15. T. A. Sanders, E. Llagostera, M. Barna, Specialized filopodia direct long-range transport of SHH during vertebrate tissue patterning. *Nature* **497**, 628–632 (2013). doi:10.1038/nature12157 Medline

16. P.-T. Chuang, T. B. Kornberg, On the range of hedgehog signaling. *Curr. Opin. Genet. Dev.* **10**, 515–522 (2000). doi:10.1016/S0959-437X(00)00121-0 Medline

17. Materials and methods and supplementary text are available as supplementary materials.

18. M. Cohen, A. Kicheva, A. Ribeiro, R. Blassberg, K. M. Page, C. P. Barnes, J. Briscoe, Ptch1 and Gli regulate Shh signalling dynamics via multiple mechanisms. *Nat. Commun.* **6**, 6709 (2015). doi:10.1038/ncomms7709 Medline

19. C. Chiang, Y. Litingtung, E. Lee, K. E. Young, J. L. Corden, H. Westphal, P. A. Beachy, Cyclopia and defective axial patterning in mice lacking Sonic hedgehog gene function. *Nature* **383**, 407–413 (1996). doi:10.1038/383407a0 Medline

20. N. Rosenfeld, M. B. Elowitz, U. Alon, Negative autoregulation speeds the response times of transcription networks. *J. Mol. Biol.* **323**, 785–793 (2002). doi:10.1016/S0022-2836(02)00994-4 Medline

21. A. Eldar, D. Rosin, B.-Z. Shilo, N. Barkai, Self-enhanced ligand degradation underlies robustness of morphogen gradients. *Dev. Cell* **5**, 635–646 (2003). doi:10.1016/S1534-5807(03)00292-2 Medline

22. B.-Z. Shilo, N. Barkai, Buffering global variability of morphogen gradients. *Dev. Cell* **40**, 429–438 (2017). doi:10.1016/j.devcel.2016.12.012 Medline

23. G. Tkačik, J. O. Dubuis, M. D. Petkova, T. Gregor, Positional information, positional error, and readout precision in morphogenesis: A mathematical framework. *Genetics* **199**, 39–59 (2015). doi:10.1534/genetics.114.171850 Medline

24. Y. Hart, U. Alon, The utility of paradoxical components in biological circuits. *Mol. Cell* **49**, 213–221 (2013). doi:10.1016/j.molcel.2013.01.004 Medline

25. J. Briscoe, Y. Chen, T. M. Jessell, G. Struhl, A hedgehog-insensitive form of patched provides evidence for direct long-range morphogen activity of sonic hedgehog in the neural tube. *Mol. Cell* **7**, 1279–1291 (2001). doi:10.1016/S1097-2765(01)00271-4 Medline

26. J. Briscoe, S. Small, Morphogen rules: Design principles of gradient-mediated embryo patterning. *Development* **142**, 3996–4009 (2015). doi:10.1242/dev.129452 Medline

27. N. Perrimon, C. Pitsouli, B.-Z. Shilo, Signaling mechanisms controlling cell fate and embryonic patterning. *Cold Spring Harb. Perspect. Biol.* **4**, a005975 (2012). doi:10.1101/cshperspect.a005975 Medline

28. Y. E. Antebi, N. Nandagopal, M. B. Elowitz, An operational view of intercellular signaling pathways. *Curr. Opin. Syst. Biol.* **1**, 16–24 (2017). doi:10.1016/j.coisb.2016.12.003 Medline

29. S. S. Gerety, M. A. Breau, N. Sasai, Q. Xu, J. Briscoe, D. G. Wilkinson, An inducible transgene expression system for zebrafish and chick. *Development* **140**, 2235–2243 (2013). doi:10.1242/dev.091520 Medline

30. R. Loew, N. Heinz, M. Hampf, H. Bujard, M. Gossen, Improved Tet-responsive promoters with minimized background expression. *BMC Biotechnol.* **10**, 81 (2010). doi:10.1186/1472-6750-10-81 Medline

31. X. Zhou, M. Vink, B. Klaver, B. Berkhout, A. T. Das, Optimization of the Tet-On system for regulated gene expression through viral evolution. *Gene Ther.* **13**, 1382–1390 (2006). doi:10.1038/sj.gt.3302780 Medline

32. A. Kicheva, P. Pantazis, T. Bollenbach, Y. Kalaidzidis, T. Bittig, F. Jülicher, M. González-Gaitán, Kinetics of morphogen gradient formation. *Science* **315**, 521–525 (2007). doi:10.1126/science.1135774 Medline

33. P. Müller, K. W. Rogers, B. M. Jordan, J. S. Lee, D. Robson, S. Ramanathan, A. F. Schier, Differential diffusivity of Nodal and Lefty underlies a reaction-diffusion patterning system. *Science* **336**, 721–724 (2012). doi:10.1126/science.1221920 Medline

34. T. Gregor, E. F. Wieschaus, A. P. McGregor, W. Bialek, D. W. Tank, Stability and nuclear dynamics of the bicoid morphogen gradient. *Cell* **130**, 141–152 (2007). doi:10.1016/j.cell.2007.05.026 Medline

35. L. Bintu, J. Yong, Y. E. Antebi, K. McCue, Y. Kazuki, N. Uno, M. Oshimura, M. B. Elowitz, Dynamics of epigenetic regulation at the single-cell level. *Science* **351**, 720–724 (2016). doi:10.1126/science.aab2956 Medline

36. E. Afgan, D. Baker, M. van den Beek, D. Blankenberg, D. Bouvier, M. Čech, J. Chilton, D. Clements, N. Coraor, C. Eberhard, B. Grüning, A. Guerler, J. Hillman-Jackson, G. Von Kuster, E. Rasche, N. Soranzo, N. Turaga, J. Taylor, A. Nekrutenko, J. Goecks, The Galaxy platform for accessible, reproducible and collaborative biomedical analyses: 2016 update. *Nucleic Acids Res.* **44**, W3–W10 (2016). doi:10.1093/nar/gkw343 Medline

37. C. Trapnell, L. Pachter, S. L. Salzberg, TopHat: Discovering splice junctions with RNA-Seq. *Bioinformatics* **25**, 1105–1111 (2009). doi:10.1093/bioinformatics/btp120 Medline

38. K. Lai, M. J. Robertson, D. V. Schaffer, The sonic hedgehog signaling system as a bistable genetic switch. *Biophys. J.* **86**, 2748–2757 (2004). doi:10.1016/S0006-3495(04)74328-3 Medline

39. K. Saha, D. V. Schaffer, Signal dynamics in Sonic hedgehog tissue patterning. *Development* **133**, 889–900 (2006). doi:10.1242/dev.02254 Medline

40. V. Marigo, R. A. Davey, Y. Zuo, J. M. Cunningham, C. J. Tabin, Biochemical evidence that patched is the Hedgehog receptor. *Nature* **384**, 176–179 (1996). doi:10.1038/384176a0 Medline

41. P. T. Chuang, A. P. McMahon, Vertebrate Hedgehog signalling modulated by induction of a Hedgehog-binding protein. *Nature* **397**, 617–621 (1999). doi:10.1038/17611 Medline

42. E. W. Humke, K. V. Dorn, L. Milenkovic, M. P. Scott, R. Rohatgi, The output of Hedgehog signaling is controlled by the dynamic association between Suppressor of Fused and the Gli proteins. *Genes Dev.* **24**, 670–682 (2010). doi:10.1101/gad.1902910 Medline

43. X. Lu, S. Liu, T. B. Kornberg, The C-terminal tail of the Hedgehog receptor Patched regulates both localization and turnover. *Genes Dev.* **20**, 2539–2551 (2006). doi:10.1101/gad.1461306 Medline

44. J. Taipale, M. K. Cooper, T. Maiti, P. A. Beachy, Patched acts catalytically to suppress the activity of Smoothened. *Nature* **418**, 892–896 (2002). doi:10.1038/nature00989 Medline

45. A. Casali, G. Struhl, Reading the Hedgehog morphogen gradient by measuring the ratio of bound to unbound Patched protein. *Nature* **431**, 76–80 (2004). doi:10.1038/nature02835 Medline

46. O. Wartlick, A. Kicheva, M. González-Gaitán, Morphogen gradient formation. *Cold Spring Harb. Perspect. Biol.* **1**, a001255 (2009). doi:10.1101/cshperspect.a001255 Medline

47. A. Uygur, J. Young, T. R. Huycke, M. Koska, J. Briscoe, C. J. Tabin, Scaling pattern to variations in size during development of the vertebrate neural tube. *Dev. Cell* **37**, 127–135 (2016). doi:10.1016/j.devcel.2016.03.024 Medline

48. J. P. Junker, K. A. Peterson, Y. Nishi, J. Mao, A. P. McMahon, A. van Oudenaarden, A predictive model of bifunctional transcription factor signaling during embryonic tissue patterning. *Dev. Cell* **31**, 448–460 (2014). doi:10.1016/j.devcel.2014.10.017 Medline

49. A. Y. Mitrophanov, E. A. Groisman, Positive feedback in cellular control systems. *BioEssays* **30**, 542–555 (2008). doi:10.1002/bies.20769 Medline

50. J. H. Levine, M. E. Fontes, J. Dworkin, M. B. Elowitz, Pulsed feedback defers cellular differentiation. *PLOS Biol.* **10**, e1001252 (2012). doi:10.1371/journal.pbio.1001252 Medline

51. F. A. Ran, P. D. Hsu, J. Wright, V. Agarwala, D. A. Scott, F. Zhang, Genome engineering using the CRISPR-Cas9 system. *Nat. Protoc.* **8**, 2281–2308 (2013). doi:10.1038/nprot.2013.143 Medline

52. L. Cong, F. A. Ran, D. Cox, S. Lin, R. Barretto, N. Habib, P. D. Hsu, X. Wu, W. Jiang, L. A. Marraffini, F. Zhang, Multiplex genome engineering using CRISPR/Cas systems. *Science* **339**, 819–823 (2013). doi:10.1126/science.1231143 Medline